

CANCER

Cancer cells produce liver metastasis via gap formation in sinusoidal endothelial cells through proinflammatory paracrine mechanisms

Truong Huu Hoang^{1,2†}, Misako Sato-Matsubara^{1,3†}, Hideto Yuasa⁴, Tsutomu Matsubara⁴, Le Thi Thanh Thuy¹, Hiroko Ikenaga¹, Dong Minh Phuong¹, Ngo Vinh Hanh¹, Vu Ngoc Hieu¹, Dinh Viet Hoang⁵, Hoang Hai¹, Yoshinori Okina¹, Masaru Enomoto¹, Akihiro Tamori¹, Atsuko Daikoku⁴, Hayato Urushima⁴, Kazuo Ikeda⁴, Ninh Quoc Dat⁶, Yutaka Yasui⁷, Hiroji Shinkawa⁸, Shoji Kubo⁸, Ryota Yamagishi⁹, Naoko Ohtani⁹, Katsutoshi Yoshizato^{3,10}, Jordi Gracia-Sancho¹¹, Norifumi Kawada^{1*}

Intracellular gap (iGap) formation in liver sinusoidal endothelial cells (LSECs) is caused by the destruction of fenestrae and appears under pathological conditions; nevertheless, their role in metastasis of cancer cells to the liver remained unexplored. We elucidated that hepatotoxin-damaged and fibrotic livers gave rise to LSECs-iGap formation, which was positively correlated with increased numbers of metastatic liver foci after intrasplenic injection of Hepa1-6 cells. Hepa1-6 cells induced interleukin-23–dependent tumor necrosis factor- α (TNF- α) secretion by LSECs and triggered LSECs-iGap formation, toward which their processes protruded to transmigrate into the liver parenchyma. TNF- α triggered depolymerization of F-actin and induced matrix metalloproteinase 9 (MMP9), intracellular adhesion molecule 1, and CXCL expression in LSECs. Blocking MMP9 activity by doxycycline or an MMP2/9 inhibitor eliminated LSECs-iGap formation and attenuated liver metastasis of Hepa1-6 cells. Overall, this study revealed that cancer cells induced LSEC-iGap formation via proinflammatory paracrine mechanisms and proposed MMP9 as a favorable target for blocking cancer cell metastasis to the liver.

INTRODUCTION

Metastasis causes approximately 90% of cancer-associated mortalities (1). The liver is the leading metastatic site of gastrointestinal malignancies, melanomas, breast cancers, and sarcomas (2) and liver itself, called intrahepatic metastasis (3). Prevention of liver metastases has always posed a great challenge to scientists. The process by which cancer cells metastasize to the liver can be divided into four major phases: (i) in the microvascular phase, tumor cells are trapped in the vasculature; (ii) in the extravascular phase, tumor cells transmigrate into the space of Disse and activate a local stromal response; (iii) in the angiogenic phase, micrometastases are vascularized; and (iv) in the growth phase, the metastases expand after tumor cells invade the liver (4). In general, each step in the metastatic cascade is related to the complex interaction between cancer cells and elements in the micro-environment. Targeting phases I and II, especially the interaction between cancer cells and liver sinusoidal endothelial cells (LSECs), is therefore important for the prevention of liver metastasis.

¹Department of Hepatology, Graduate School of Medicine, Osaka Metropolitan University, Osaka, Japan. ²Department of Pain Medicine and Palliative Care, Cancer Institute, 108 Military Central Hospital, Hanoi, Vietnam. ³Endowed Laboratory of Synthetic Biology, Graduate School of Medicine, Osaka Metropolitan University, Osaka, Japan. ⁴Department of Anatomy and Regenerative Biology, Graduate School of Medicine, Osaka Metropolitan University, Osaka, Japan. ⁵Department of Anesthesiology, Cho Ray Hospital, Ho Chi Minh City, Vietnam. ⁶Department of Pediatrics, Hanoi Medical University, Hanoi, Vietnam. ⁷Department of Gastroenterology and Hepatology, Musashino Red Cross Hospital, Tokyo, Japan. ⁸Department of Hepato-Biliary-Pancreatic Surgery, Graduate School of Medicine, Osaka Metropolitan University, Osaka, Japan. ⁹Department of Pathophysiology, Graduate School of Medicine, Osaka Metropolitan University, Osaka, Japan. ¹⁰BiolIntelligence Co. Ltd., Osaka, Japan. ¹¹Liver Vascular Biology Research Group, IDIBAPS Biomedical Research Institute, CIBEREHD, Barcelona, Spain.

*Corresponding author. Email: kawadanori@omu.ac.jp

†These authors contributed equally to this work.

For more than two decades, much research has been conducted to better understand the interaction between cancer cells and LSECs. In vitro coculture experiments, cancer cells induced an “activated” phenotype of LSECs by modifying genes related to proliferation, migration, and tube formation (5), ultimately resulting in angiogenesis (6). Activated LSECs produce cytokines such as tumor necrosis factor- α (TNF- α), interleukins, and transforming growth factor- β , which play a role in the recruitment and activation of immune cells that contribute to metastasis progression (7). In some animal models, pretreatment with TNF- α increases liver metastasis by inducing adhesion molecules such as E-selectin, intracellular adhesion molecule 1 (ICAM1), and vascular adhesion molecule 1 in LSECs, which promotes transendothelial migration (T.E.M.) of tumor cells (8, 9). Furthermore, anti-ICAM1 antibody treatment notably inhibits tumor cell adhesion to LSECs via Notch signaling in mice (10). Thus far, many strategies and medicines have been proposed to modulate LSEC phenotypes or functions to inhibit liver metastasis in clinical settings, but success has been limited.

LSECs are highly specialized endothelial cells with unique morphology and function. They contain many pores (fenestrae) approximately 100 to 150 nm in diameter and thus provide an open channel between sinusoidal nutrient-rich blood and the subepithelial space of Disse (11, 12). LSECs are involved in the mechanism of hepatic immune tolerance (7), which is modulated by immune checkpoint molecules such as PD-L1 (Programmed death-ligand 1) (13). During some pathological conditions, LSECs undergo “capillarization,” a dedifferentiation process characterized by loss of fenestration and acquisition of a vascular phenotype (14, 15). Fenestrated LSECs maintain hepatic stellate cell quiescence, whereas capillarized LSECs precede liver fibrosis (16, 17). In addition, the destruction or coalescence of fenestrae in LSECs has been reported to give rise to intracellular

Copyright © 2022
The Authors, some
rights reserved;
exclusive licensee
American Association
for the Advancement
of Science. No claim to
original U.S. Government
Works. Distributed
under a Creative
Commons Attribution
NonCommercial
License 4.0 (CC BY-NC).

Downloaded from https://www.science.org on June 12, 2023

gaps (iGaps) with pore sizes of more than 250 nm (18, 19). Formation of iGap in LSECs (hereinafter referred to as LSECs-iGap) induced by high doses of chemicals, such as pyrrolizidine alkaloids (20, 21), monocrotaline (MCT) (22), and acetaminophen (APAP) (23, 24), is a characteristic of the early stages of hepatic sinusoidal obstruction syndrome (SOS). Activation of matrix metalloproteinases (MMPs) is reportedly involved in LSECs-iGap formation, and administration of MMP inhibitors reduces LSECs-iGap (25) and attenuates LSEC damage and hemorrhage in the liver in an MCT-induced SOS mouse model (26). Thus, LSECs-iGap is frequently observed in animal models and is closely associated with liver damage during chemotherapy, while the role of LSECs-iGap in liver metastases remains to be elucidated.

Here, we performed a functional analysis of LSECs-iGap formation induced by hepatotoxins or interactions with Hepa1-6 cancer cells to evaluate their role in liver metastasis. Using image analyses in various mouse models, we demonstrate that cancer cells directly broke through the LSECs-iGap, both in vitro and in vivo. We also show that interleukin-23 (IL-23), TNF- α , MMP9, and ICAM1 were involved in LSECs-iGap formation caused by the interaction between cancer cells and LSECs and that inhibition of MMP9 significantly reduced LSEC-iGap formation and hepatic metastasis. Our findings provide new insights into cancer cell extravasation in the liver via LSECs-iGap and may lead to novel strategies to prevent liver metastasis.

RESULTS

iGap formation in LSECs positively correlates with liver metastasis

Given the unique features of LSECs with the appearance of fenestration and iGap formation under some pathological conditions common to humans and mice, we hypothesized that LSECs-iGap might facilitate the penetration of cancer cells into the liver parenchyma. Two different experimental approaches were used (Fig. 1A). We first induced LSECs-iGap in mice by intraperitoneal injection of APAP (27), followed by intrasplenic injection of Hepa1-6 cells [2×10^6 cells in Dulbecco's modified Eagle's medium (DMEM)], and examined the formation of metastatic tumor foci in the livers by hematoxylin and eosin (H&E) staining after 3 days. The results showed that APAP pretreatment significantly increased LSECs-iGap formation (Fig. 1B) and the number of tumor foci in the liver (Fig. 1C). These results suggest a positive correlation between LSECs-iGap formation and liver metastasis.

To further confirm the relationship between LSECs-iGap formation and liver metastasis, we conducted a second in vivo mouse experiment using the thioacetamide (TAA)-induced liver fibrosis model. After 12 weeks of TAA treatment, the appearance of sinusoidal lumen in nonfibrotic areas of the liver was different from that in fibrotic areas around the central vein of the liver. In the fibrotic areas, defenestration and capillarization were observed, whereas LSECs-iGap formation was prominent in the nonfibrotic areas. The mean number of LSECs-iGap per $100 \mu\text{m}^2$ in the nonfibrotic areas was significantly higher than that in the fibrotic areas (Fig. 1D and fig. S1A). Because these features of LSECs under different conditions of hepatic fibrosis might alter the metastatic capacity of cancer cells, we next examined the number of tumor foci in the liver at 5 days after intrasplenic injection of Hepa1-6 cells. H&E and Sirius Red staining showed that the tumor foci mostly appeared in nonfibrotic

areas rather than in fibrotic areas (Fig. 1E). These results further suggest that the presence of LSECs-iGap promotes liver metastasis of Hepa1-6 cells.

Following our observations in mouse models, we next asked whether LSECs-iGap appeared in humans. We observed LSECs-iGap using transmission electron microscopy (TEM) in liver biopsy specimens from patients with chronic hepatitis C who sustained virological responses to antiviral therapies, with different stages of liver fibrosis (fig. S1B). Human LSECs in nonfibrotic areas adjacent to collagen-deposited regions displayed significantly more LSECs-iGap than those in nonfibrotic livers (Fig. 1F and fig. S1, C and D).

Cancer cells invade the liver directly through iGap in LSECs

Because intrasplenic injection of Hepa1-6 cells is an established in vivo mouse model for liver tumorigenesis, we speculated that cancer cells might directly induce LSECs-iGap formation. There was a significant increase in LSECs-iGap in the Hepa1-6 cell-injected group compared to the control group (Fig. 2A and fig. S2A). Next, we conducted in vitro and in vivo experiments to show that LSECs-iGap formation is associated with liver metastasis. Because the interaction between Hepa1-6 cells and LSECs is expected to occur at an early stage of liver metastasis, we fixed and analyzed livers at 18 hours after splenic injection of Hepa1-6 cells (Fig. 2B). The Hepa1-6 cells were morphologically distinct from other cell types in the liver (i.e., lymphocytes, monocyte-derived macrophages, and Kupffer cells) in scanning electron microscopy (SEM) images (fig. S2B). Furthermore, Hepa1-6 cells were characterized by more abundant mitochondria in the cytoplasm compared with macrophages in the TEM images (fig. S2C). It was still a challenge to distinguish Hepa1-6 cells from macrophages in SEM images, so we used clodronate liposomes (CLs) to remove macrophages before image analysis (fig. S2D). The results provide direct evidence that Hepa1-6 cells can protrude into LSECs-iGap (Fig. 2C). Immunofluorescence staining with the tumor marker alpha-fetoprotein and the endothelial marker CD31 showed that a single Hepa1-6 cell could disrupt LSECs and invade the liver parenchyma (Fig. 2D). Furthermore, we frequently observed the appearance of LSECs-iGap in liver sinusoids after intrasplenic injection of other types of murine cancer cells, including 4T1 breast cancer cells and Colon26 colon cancer cells (fig. S2, E and F).

To more thoroughly analyze the interaction between cancer cells and LSECs in the liver, we conducted three-dimensional (3D) tomography reconstruction (3D-TR), which automatically acquires continuous tissue sections for 3D imaging. The resulting 3D images showed liver sections with Hepa1-6 cells, hepatocytes, and sinusoidal lumen labeled yellow, green, and purple, respectively (Fig. 2E). We observed a Hepa1-6 cell in close contact with a hepatocyte, with a part of the Hepa1-6 cell located in the liver parenchyma and the rest in the sinusoidal lumen. Notably, we found a broken LSEC by Hepa1-6 cell with a distance of approximately $3 \mu\text{m}$ (Fig. 2F). The 3D structures clearly showed the Hepa1-6 cell penetrating a single LSEC, suggesting that Hepa1-6 cells can invade the liver parenchyma via LSECs-iGap, rather than by passing through the intercellular space between separate LSECs (Fig. 2, G and H, and movies S1 and S2). Furthermore, using in vitro migration experiments, cocultured Hepa1-6 cells migrated via LSECs-iGap (Fig. 2, I and J). Together, our results provide evidence that direct association of LSECs with Hepa1-6 cells leads to the formation of LSECs-iGap, which constitutes the extravascular phase of cancer cell metastasis in the liver sinusoid.

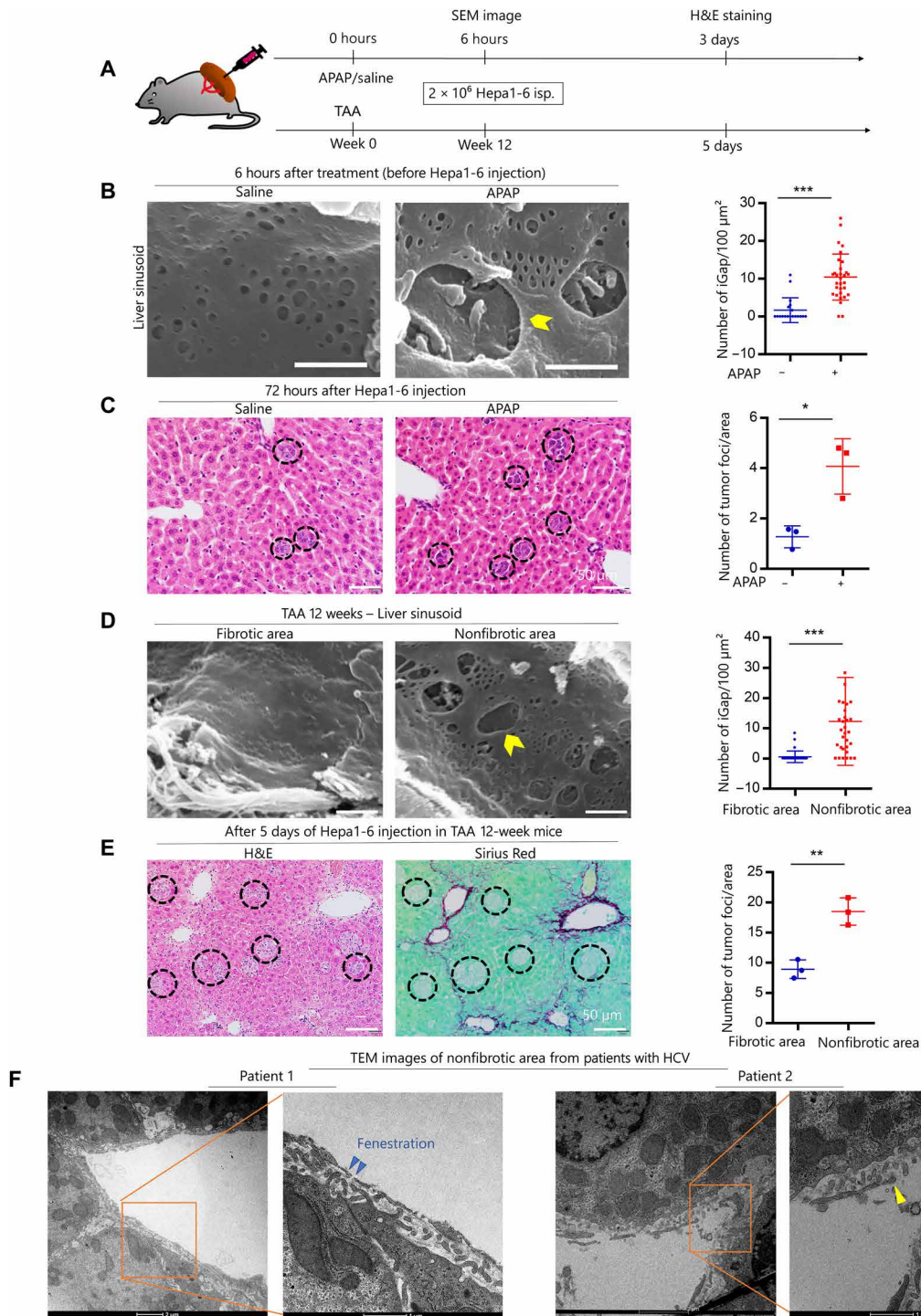


Fig. 1. Association of cancer cell invasion with chemically and fibrosis-induced LSECs-iGap. (A) Schematic model of APAP/saline, thioacetamide (TAA) treatment, and liver metastasis using Hepa1-6 cell implantation in mouse spleens. (B) scanning electron microscopy (SEM) images show liver sinusoid 6 hours after intraperitoneal APAP or saline injection and quantification of the average number of LSECs-iGap per 100 μm². Scale bar, 800 nm. (C) H&E staining shows multiple tumor foci (black circles) in the liver 3 days after Hepa1-6 cell injection. The average number of tumor foci per unit area. Scale bar, 50 μm. (D) SEM images show fibrotic and nonfibrotic areas in the liver sinusoid 12 weeks after TAA induction of liver fibrosis. Quantification of the average number of LSECs-iGap per 100 μm². Scale bar, 800 nm. (E) Representative H&E (left) and Sirius Red (right) staining show tumor foci (black circles) in the liver 5 days after Hepa1-6 cell injection given 12 weeks after TAA injection. Scale bar, 50 μm. The average number of tumor foci was quantified in the fibrotic or nonfibrotic area. (F) Representative TEM images show LSECs-iGap in nonfibrotic areas of livers in patients with HCV (hepatitis C virus) infection and liver fibrosis. An enlarged view of the TEM image shows fenestration (blue arrowhead) and LSECs-iGap (yellow arrowhead) of approximately 150 nm and 1 μm in diameter, respectively. Scale bar, 1 μm. All quantification data are from at least 25 random fields and presented as the means ± SD. N = 3 independent experiments for each triplicate per group. *P < 0.05, **P < 0.01, and ***P < 0.001, two-tailed unpaired Student's *t* tests.

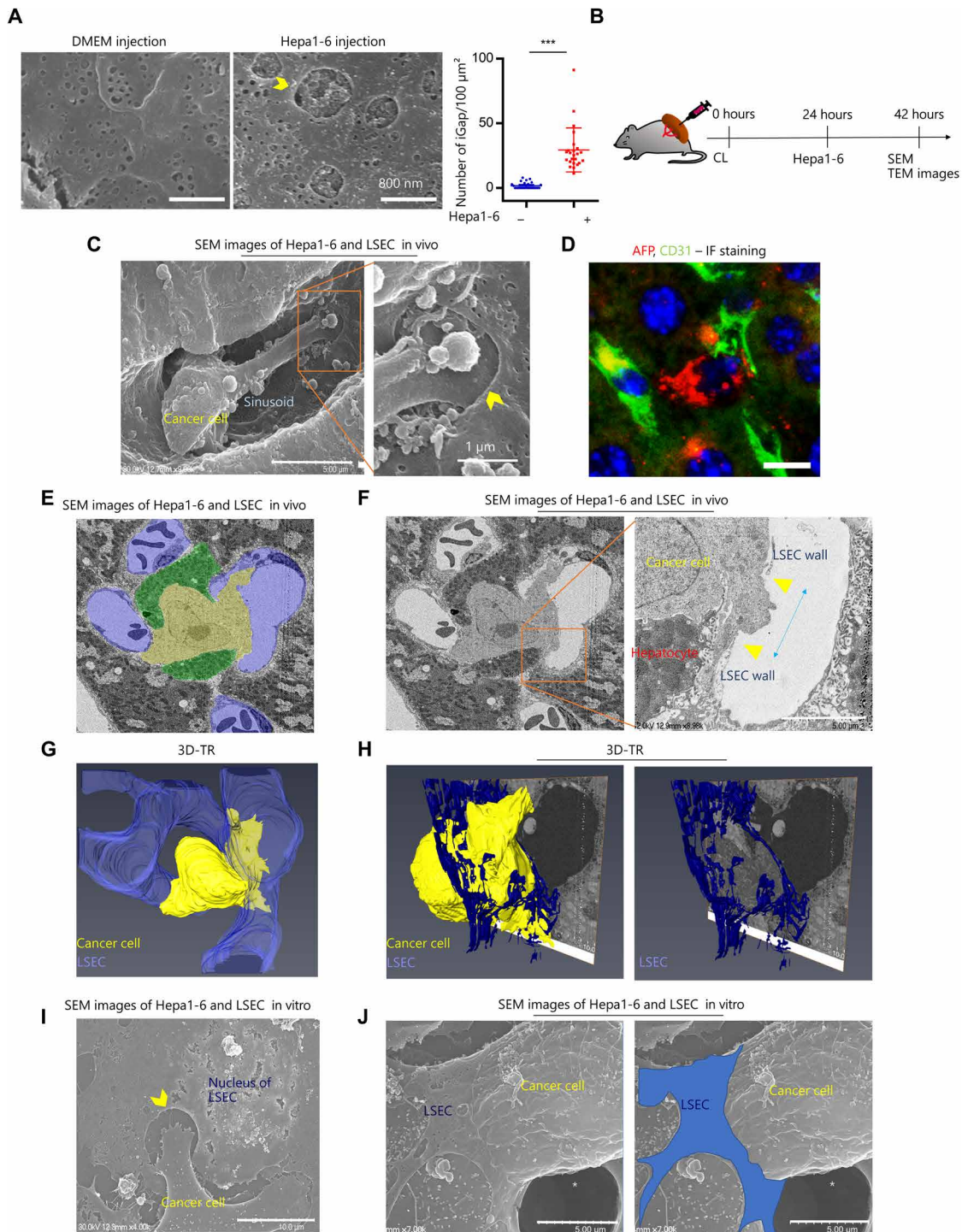


Fig. 2. Image analysis of cancer cell invasion via LSECs-iGap. (A) Representative SEM images of LSECs-iGap in mouse liver sinusoid 24 hours after intrasplenic injection of Hepa1-6 cells and the average number of LSECs-iGap per $100 \mu\text{m}^2$. Scale bars, 800 nm. LSECs-iGap was quantified from at least 25 random fields, $N = 3$ per group. Data are shown as means \pm SD. *** $P < 0.001$, two-tailed unpaired Student's t test. (B) Schematic model of intrasplenic injection of Hepa1-6 cells for liver metastases after clodronate liposome injection. (C) Representative SEM images show Hepa1-6 cells invading into the LSECs-iGap. Scale bars, 5 μm (left) and 1 μm (right). (D) Immunofluorescence (IF) staining for Hepa1-6 cells and LSECs with alpha-fetoprotein (AFP; red) and CD31 (green), respectively. 4',6-Diamidino-2-phenylindole (DAPI) (blue) for nuclei. Scale bar, 20 μm . (E and F) In vivo SEM images show the interactions among Hepa1-6 cells (yellow), hepatocytes (green), and LSECs (purple). (F) Enlarged view of a Hepa1-6 cell (right) penetrating an LSEC; blue arrow indicates the LSECs-iGap approximately 3 μm in diameter. Scale bar, 5 μm . (G and H) A 3D-TR image of (E) shows the Hepa1-6 cell breaking through the lumen of the sinusoid. The LSEC and the Hepa1-6 cell are colored blue and yellow, respectively. (I and J) In vitro SEM image of a Hepa1-6 cell and an LSEC under coculture conditions. White asterisk indicates pore of insert. (I) Hepa1-6 cell extends a protrusion into the LSECs-iGap. (J) The Hepa1-6 cell penetrating an LSEC (blue). Scale bars, 10 (left) and 5 μm (right). Yellow arrowheads indicate LSECs-iGap.

MMP9 is involved LSECs-iGap after interaction between LSECs and cancer cells

We hypothesized that the interaction of cancer cells with LSECs induces the formation of LSECs-iGap. To verify our hypothesis, we designed an in vitro experiment using an insert coculture system in which Hepa1-6 cells and LSECs were separately cocultured for 24 hours and subsequently analyzed (Fig. 3A). We confirmed that LSECs cocultured with Hepa1-6 cells had more iGap compared with monocultured LSECs (Fig. 3B), which were consistent with the results of our in vivo mouse experiments. In contrast, LSECs cocultured with primary mouse hepatocytes, as a nonmetastatic control, failed to display LSECs-iGap (fig. S3A). We next performed RNA sequencing (RNA-seq) analysis in cocultured and monocultured LSECs. A partial least squares–discriminant analysis (PLS-DA) score plot using fragment per kilobase of exon per million reads mapped (FPKM) values for 13,525 genes showed segregation of gene clusters between cocultured and monocultured LSECs, but there was less segregation of the Hepa1-6 cell gene clusters (fig. S3B and data S1). Hierarchical clustering analysis of 553 differentially expressed genes (DEGs) revealed two distinct clusters of cocultured and monocultured LSECs (Fig. 3C). This analysis showed that *Mmp9* was a top up-regulated gene in the cocultured LSECs, with nearly 100-fold higher expression than in monocultured LSECs (data S2). Using the results of RNA-seq analysis, we evaluated whether the increased MMP9 expression was associated with LSECs-iGap formation. Reverse transcription polymerase chain reaction (RT-PCR) confirmed that *Mmp9* expression was significantly increased in LSECs cocultured with Hepa1-6 cells compared with that in monocultured LSECs. However, *Mmp9* expression in Hepa1-6 cells did not change under any culture conditions (Fig. 3D). In addition, MMP9 activity increased in the culture medium from LSECs cocultured with Hepa1-6 cells compared with that in medium from monocultured LSECs (Fig. 3E). Although MMP2 was previously reported to be involved in chemically induced LSECs-iGap formation (25), we did not observe any changes in MMP2 mRNA or protein levels in murine LSECs (fig. S3C). To examine the role of MMP9 in LSECs-iGap formation, we conducted in vitro experiments in which LSECs were pretreated with the MMP inhibitor doxycycline (DOX) for 2 hours, washed, and then cocultured with Hepa1-6 cells. The results showed that LSECs-iGap formation was significantly reduced by DOX pretreatment compared with that in untreated LSECs (Fig. 3F).

Next, the effect of MMP2/9 inhibitor was tested using a mouse model by intrasplenic injection of Hepa1-6 cells. As shown in Fig. 2A, we confirmed that the number of LSECs-iGap was significantly increased in the Hepa1-6–injected mice compared with that in the control mice. In addition, MMP9 activity was increased in liver lysates from the Hepa1-6–injected mice compared with that in liver lysates from control mice (Fig. 3G), suggesting the involvement of MMP9 activity in LSECs-iGap formation. Moreover, we blocked MMP9 activity using *N*-[(1,1'-biphenyl)-4-ylsulfonyl]-*D*-phenylalanine, the MMP2/9 inhibitor. We counted the number of LSECs-iGap and tumor foci in mouse livers by SEM analysis on day 1 and by H&E staining on day 5, respectively. The SEM images showed a remarkable reduction of LSEC-iGap formation in the MMP2/9 inhibitor–treated mice when compared with that in the control group (Fig. 3H). Accordingly, liver engraftment of Hepa1-6 cells was also reduced in the MMP2/9 inhibitor–treated mice compared with that in the control mice (Fig. 3I).

To determine the function of MMP9 in LSEC-iGap formation, we used lentiviral short hairpin RNA (shRNA) to knock down *Mmp9* (shMMP9) or *GFP* [short hairpin green fluorescent protein (shGFP)] as a control in LSECs (Fig. 3J) and performed a T.E.M. assay. For the T.E.M. assay, LSECs were first cultured on inserts. The next day, Hepa1-6 cells were seeded on the monolayer of LSECs (Fig. 3K). After 24 hours, Hepa1-6 cells that migrated across the LSEC layer were stained with crystal violet. The penetration of Hepa1-6 in the iGap during T.E.M. performance has no direct evidence. However, we found that migration of the Hepa1-6 cells was largely reduced across the shMMP9-LSECs compared with that across the shGFP-LSECs (Fig. 3L). Similar to chemically induced LSECs-iGap, they were induced by the interaction of Hepa1-6 cells with LSECs via MMP9. MMP9 activity was remarkably elevated in conditioned medium from direct cocultures between LSEC–Hepa1-6 and human umbilical endothelial cell (HUVEC)–HepG2 (Hepatoma G2), a human hepatocellular carcinoma (HCC) cell line, compared with that in conditioned media from indirect cocultures using inserts (fig. S3D). These results indicate that the interaction between the Hepa1-6 cells and LSECs was much more robust when there was direct cell-to-cell contact.

Interaction between cancer cells and LSECs dominantly induces the TNF- α signaling pathway, causing induction of MMP9 and ICAM1 expression in LSECs

Because Hepa1-6 cells accelerated LSECs-iGap formation via MMP9 activity, we performed gene ontology (GO) enrichment analysis using Enrichr software to identify the signaling pathways involved. The RNA-seq dataset revealed 289 genes that were up-regulated in LSECs cocultured with Hepa1-6 cells when compared with monocultured LSECs (≥ 2 -fold change in expression, $P > 0.05$; data S3). The functional annotation of these DEGs based on the Molecular Signature Database and the Kyoto Encyclopedia of Genes and Genomes Hallmark Pathways indicated over representation of genes involved in TNF- α signaling (Fig. 4A and fig. S4A). We therefore speculated that TNF- α signaling is involved in LSECs-iGap formation. Under cocultured conditions, *Tnf- α* mRNA was increased in LSECs but not in Hepa1-6 cells (Fig. 4B and fig. S4B). Other up-regulated genes involved in TNF- α signaling including *Mmp9* (Fig. 3D), *Chemokine (C-X-C motif) ligand 1 (Cxcl1)*, *Cxcl2*, *Cxcl5*, and *Icam1* were validated by RT-PCR and found to be significantly increased in LSECs cocultured with Hepa1-6 cells when compared with monocultured LSECs cocultured with primary mouse hepatocytes (Fig. 4B and fig. S4C). TNF- α protein was also present in conditioned medium from the cocultured LSECs and Hepa1-6 cells but not in combined media from monocultured LSECs and Hepa1-6 cells (Fig. 4C). To verify that TNF- α can induce the identified DEGs in LSECs, we treated LSECs with recombinant mouse (rm) TNF- α , which showed a time-dependent phosphorylation of nuclear factor κ B (NF- κ B), followed by increased mRNA expression of *Mmp9* and *Icam1*, but not *Mmp2*, in LSECs at 24 hours (Fig. 4, D and E, and fig. S4D).

To determine which molecules derived from Hepa1-6 cells can induce TNF- α , we used cytokine arrays to identify proteins in conditioned medium from cocultured Hepa1-6 cells and LSECs and in combined media from monocultures of LSECs and Hepa1-6 cells. The results showed that the five most up-regulated proteins in the coculture medium compared with the single culture medium were TNF- α , IL-23, colony-stimulating factor 1, growth differentiation factor 15, and CXCL10 (Fig. 4F and fig. S4E). Of these genes, *Il23*

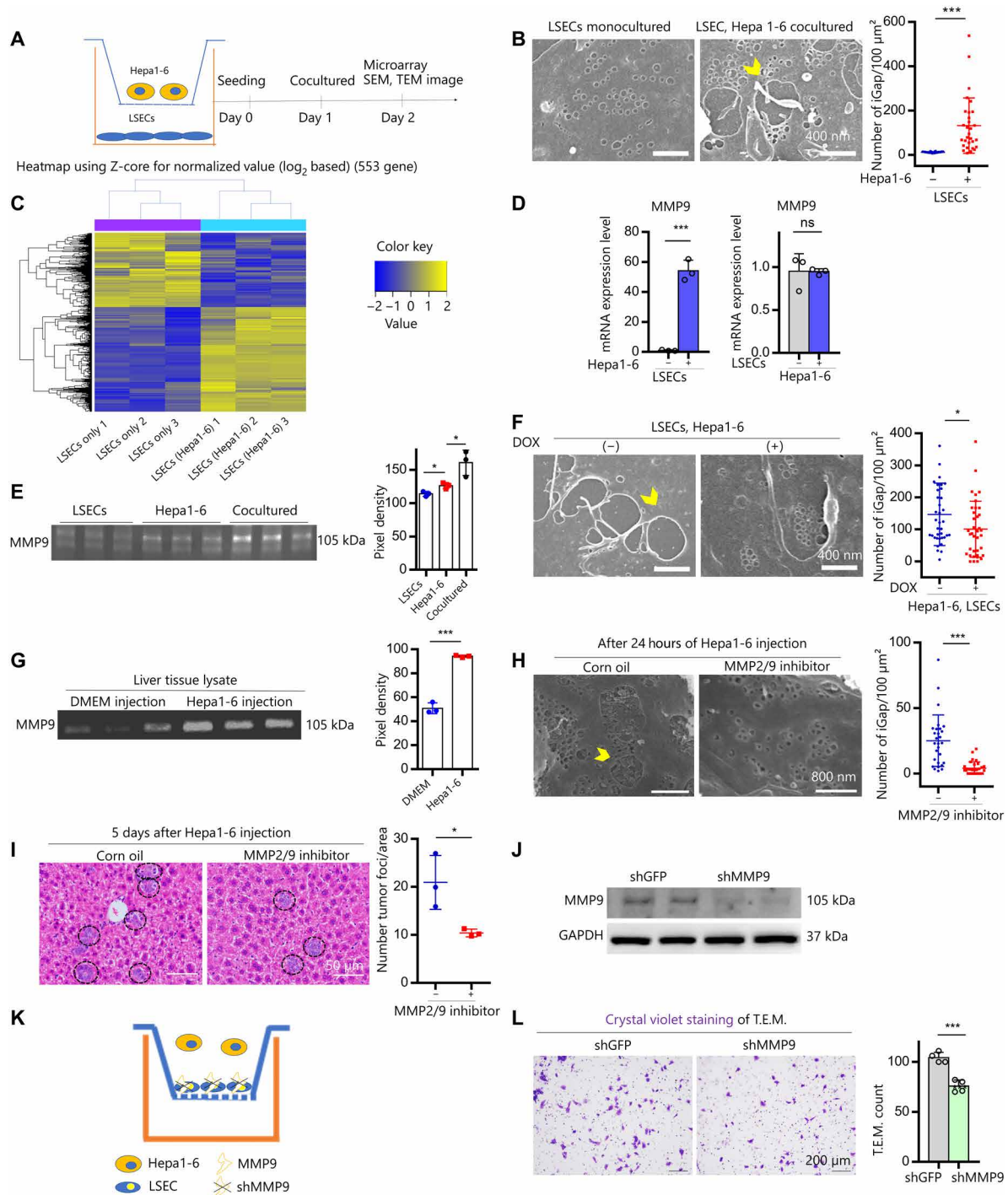


Fig. 3. Effects of MMP9 activity on cancer cell transmigration via LSECs-iGap. (A) Scheme of the transwell system separating LSECs (bottom) from Hepa1-6 cells (inset). (B) Representative SEM images of monocultured LSECs and cocultured LSEC–Hepa1-6 cells after 24 hours. Scale bars, 400 nm. (C) Heatmap of DEGs (553 genes, >2-fold expression change, $P < 0.05$) between monocultured LSECs and cocultured LSEC–Hepa1-6 cells. (D) MMP9 mRNA expression by quantitative RT-PCR (qRT-PCR) in LSECs (left) and Hepa1-6 cells (right). ns, not significant. (E) MMP9 activity in conditioned medium from LSEC and Hepa1-6 cell mono- and cocultures. (F) Representative SEM images of LSECs-iGap after 24 hours of coculture with Hepa1-6 cells with or without DOX pretreatment. Scale bars, 400 nm. (G) MMP9 activity in liver lysates from DMEM (control) or Hepa1-6 cell-injected mice. (H) Representative SEM images of LSECs-iGap after intrasplenic injection of Hepa1-6 cells with or without MMP2/9 inhibitor. Scale bars, 800 nm. (I) Representative H&E staining of tumor foci (black circles) in liver 3 days after intrasplenic injection of Hepa1-6 cells. Scale bars, 50 μ m. (J) Immunoblots of MMP9 in LSECs transfected with shGFP (control) or shMMP9. GAPDH, glyceraldehyde phosphate dehydrogenase. (K and L) Diagram (K), images, and quantification (L) of T.E.M. assays; Hepa1-6 cells transmigrate through an LSEC monolayer. Average number of tumor foci per area (I) and LSECs-iGap per 100 μ m² (B, F, and H). Gelatin zymography was quantified with pixel density (E and G), $N = 3$ per group. Yellow arrowheads indicate LSECs-iGaps. Data are shown as means \pm SD. * $P < 0.05$ and *** $P < 0.001$, two-tailed unpaired Student's t tests and one-way analysis of variance (ANOVA) (E).

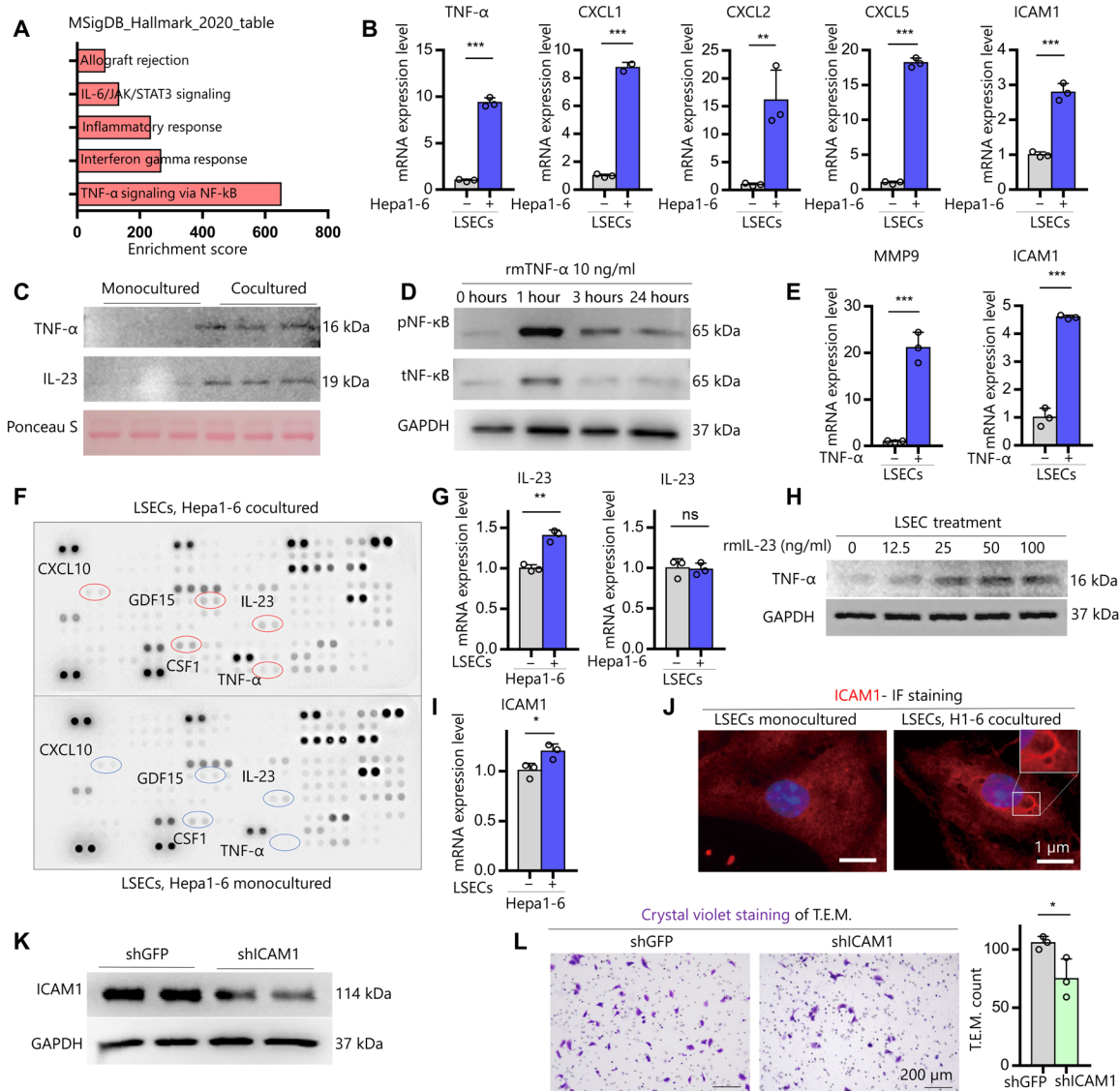


Fig. 4. IL-23 derived from Hepa1-6 cells promotes the TNF- α signaling pathway and induces MMP9 and ICAM1 expression in LSECs. (A) DEGs in cocultured LSECs were functionally classified according to Molecular Signature Database (MSigDB) Hallmark 2020. JAK, Janus kinase; STAT3, signal transducer and activator of transcription 3. (B) Validation by qRT-PCR of the TNF- α signaling pathway-related gene expression in LSECs cocultured with Hepa1-6 cells. (C) Immunoblots for TNF- α and IL-23 in media from monocultured LSECs and cocultured LSEC-Hepa1-6 cells. Ponceau S, loading control. (D) Immunoblots of phosphorylated and total NF- κ B (pNF- κ B and tNF- κ B, respectively) in LSECs treated with rmTNF- α (10 ng/ml) in a time-dependent manner. (E) qRT-PCR analysis of MMP9 and ICAM1 in LSECs treated with rmTNF- α (10 ng/ml) for 24 hours. (F) Cytokine array for soluble factors in combined media from monocultured LSECs and Hepa1-6 cells and in medium from cocultured LSECs and Hepa1-6 cells. The soluble factors with the biggest change are circled. (G) qRT-PCR analysis of IL-23 in Hepa1-6 cells (left) and LSECs (right) under coculture conditions. (H) Immunoblots of TNF- α in LSECs treated with rmlIL-23 in a dose-dependent manner. (I) qRT-PCR analysis of iCAM1 expression in monocultured LSECs and LSECs cocultured with Hepa1-6 cells for 24 hours. (J) Representative IF of ICAM1 staining in LSECs. Scale bar, 1 μ m. (K) Immunoblots of ICAM1 protein in primary mouse LSECs transfected with shGFP (control) or shICAM1. (L) Representative images and quantification of Hepa1-6 cells that migrated through transwell inserts coated with shGFP-LSECs or shICAM1-LSECs in T.E.M. assays. GAPDH, loading control (D and K). Data are shown as means \pm SD; * P < 0.05, ** P < 0.01, and *** P < 0.001, two-tailed unpaired Student's t tests.

mRNA was significantly up-regulated by Hepa1-6 cells but not by LSECs (Fig. 4G and fig. S4F). IL-23 expression was subsequently validated and detected in the cocultured medium (Fig. 4C). Furthermore, rmlIL-23 promoted dose-dependent secretion of TNF- α in LSECs after 24 hours (Fig. 4H). These results suggest that IL-23 from Hepa1-6 cells stimulates LSECs to produce TNF- α , which subsequently induces downstream target genes, including *Mmp9* and *Icam1*.

The results of the GO analysis revealed that up-regulated DEGs in cocultured LSECs were significantly enriched with molecular functions involved in “binding” and with cellular components including “cytoplasm” and “membrane” (fig. S4G). ICAM1 is a well-known adhesion molecule expressed in LSECs that functions in endothelial cell-mediated cancer cell invasion (28). Because ICAM1 was another candidate from significantly up-regulated TNF- α family genes in the list of RNA-seq (Fig. 4, B and E), we further

investigated its function in the interaction between Hepa1-6 cells and LSECs. *Icam1* expression was significantly elevated in both cocultured LSECs and Hepa1-6 cells (Fig. 4, B and I) and also in HUVECs cocultured with HepG2 cells (fig. S4H), suggesting that ICAM1 might be involved in cell-cell binding. Notably, ICAM1 was selectively expressed at the edge of LSECs-iGap under coculture conditions (Fig. 4J). To evaluate the functional role of ICAM1 expression in LSECs, we knocked down *Icam1* (shICAM1) in LSECs (Fig. 4K) and performed T.E.M. assays (fig. S4I). The number of migrated Hepa1-6 cells in cocultures with shICAM1-LSECs was significantly reduced compared with that in coculture with control shGFP-LSECs (Fig. 4L). Overall, these data demonstrate that secretion of IL-23 by Hepa1-6 cells promotes TNF- α production in LSECs, which leads to increased expression of MMP9 and ICAM1 via phosphorylation of NF- κ B, resulting in LSECs-iGap formation.

TNF- α induces iGap formation due to depolymerization of F-actin in LSECs

LSEC fenestration is thought to be regulated by the action of numerous molecules on the actin cytoskeleton (29); therefore, phalloidin staining and SEM imaging analyses were performed to determine whether LSECs-iGap formation is attributed to F-actin depolymerization. First, we demonstrated that cytochalasin D (CytoD), a polymerization inhibitor, blocked actin assembly and induced LSECs-iGap formation (Fig. 5A). Likewise, treatment with rmTNF- α significantly reduced phalloidin positivity and increased the number of LSECs-iGap (Fig. 5B). Last, we found that F-actin expression was significantly diminished and markedly disorganized in LSECs cocultured with Hepa1-6 cells compared with that in monocultured LSECs, suggesting that F-actin depolymerization was induced by Hepa1-6–derived paracrine effectors (Fig. 5B). Addition of anti-TNF- α antibody clearly preserved F-actin structures and inhibited LSECs-iGap formation (Fig. 5C). Furthermore, TNF- α was significantly increased in the liver lysates of mice treated with APAP for 6 hours, corresponding with LSECs-iGap appearance as shown in Fig. 1C (fig. S5A). Together, these results confirmed that TNF- α induces LSECs-iGap formation as a result of actin disassembly.

MMP9 and ICAM1 expression are associated with intrahepatic metastasis and survival outcomes in patients with HCC

To explore whether TNF- α signaling–induced LSECs-iGap formation may be a valid target for metastasis prevention, we further evaluated the clinical relevance of ICAM1 and MMP9 expression in patients with HCCs. Immunohistochemical (IHC) staining was performed using diagnosed HCC with vascular invasion, which strongly correlates with the presence of intrahepatic metastasis, due to the limited number of surgically resected samples for metastatic cancers from distant organs (3, 30). We performed IHC staining to analyze the expression of ICAM1 and MMP9 in resected tumor samples from 98 patients with HCC. First, we confirmed that ICAM1 expression shared the same pattern as eNOS (endothelial nitric oxide synthase) expression, a marker of endothelial cells (fig. S6A) (31). We also confirmed that MMP9 was expressed in hepatocytes, inflammatory cells, and endothelial cells (fig. S6B). Expression of ICAM1 and MMP9 in the samples was divided into four groups: weak, medium, strong, or strongest, according to the percentage of positive staining per field as described in Materials and Methods (Fig. 6A). Some tumors with vascular invasion were positive for

both ICAM1 and MMP9 (fig. S6C). Univariate logistic regression revealed that high ICAM1 expression [odds ratio (OR): 4.67, 95% confidence interval (CI): 1.67 to 13.01; $P = 0.003$] and either high ICAM1 or high MMP9 expression (OR: 4.62; 95% CI: 1.80 to 11.82; $P = 0.001$) were associated with vascular invasion. Multivariate logistic regression adjusted for Child-Pugh scores and tumor sizes indicated that high ICAM1 expression (OR: 3.36; 95% CI: 1.13 to 10.00; $P = 0.03$) and either high ICAM1 or high MMP9 expression (OR: 4.31; 95% CI: 1.57 to 11.80; $P = 0.005$) were independently associated with vascular invasion (table S1 and statistical analysis of clinical data are shown in table S3). High ICAM1 expression and combined high ICAM1 and MMP9 expression were correlated with poor overall survival (Fig. 6B and table S2). Furthermore, there was a positive correlation between high MMP9 expression and the risk of recurrence (fig. S6D and table S4).

Treatment with MMP inhibitors reduces LSECs-iGap formation and attenuates liver metastasis

We next aimed to demonstrate the effect of MMP9 inhibition on chemically induced LSECs-iGap formation and subsequent liver metastasis. MCT is known as an MMP inducer, and intraperitoneal injection of MCT induces SOS in mice (26). Therefore, we first tested whether MCT could induce LSECs-iGap formation in vitro (Fig. 7A). MCT resulted in the increased appearance of LSECs-iGap compared with vehicle-treated cells, which was prevented by DOX treatment (Fig. 7B). We measured MMP9 activities in the conditioned media and cell lysates from these experiments, which showed that after 4 hours of MCT treatment, MMP9 activity was slightly increased, while it was clearly blocked in the presence of DOX in the conditioned medium (fig. S7A). In contrast to the conditioned medium, we saw a marked increase in MMP9 activity in cell lysates from MCT-treated LSECs compared with that in control lysates (Fig. 7C). Together, these results support our hypothesis that MMP9 plays an important role in LSECs-iGap formation.

Last, we performed in vivo allogeneic transplant experiments as described in Fig. 7D. Two days after a single intragastric gavage of MCT, LSECs of the treated mice displayed a notable number of iGap when compared with those that received saline (control) or DOX, but the number and porosity of the iGap were remarkably lower in LSECs of mice treated with DOX/MCT (Fig. 7, E to G). Consistent with the appearance of LSECs-iGap, the number of tumor foci in the livers of MCT-treated mice was significantly increased, when compared with that in the control mice. In contrast, the number of tumor foci was significantly reduced in the MCT/DOX-treated mice compared with that in the MCT-treated mice (Fig. 7H).

Together, in LSECs interacted with Hepa1-6 cells, IL-23–induced TNF- α expression promoted F-actin depolymerization and the expression of MMP9, as well as ICAM1 and proinflammatory cytokines, resulting in LSECs-iGap formation to facilitate liver metastasis. Inhibition of LSECs-iGap formation by blocking MMP9 activity significantly reduced liver metastasis, demonstrating the effectiveness of targeting LSECs-iGap formation with MMP9 inhibitors to prevent metastasis (Fig. 7I).

DISCUSSION

Endothelial cells are the first barrier through which transmigrating tumor cells must pass. It is widely accepted that a common mechanism of metastasis is a process involving cell rearrangement and

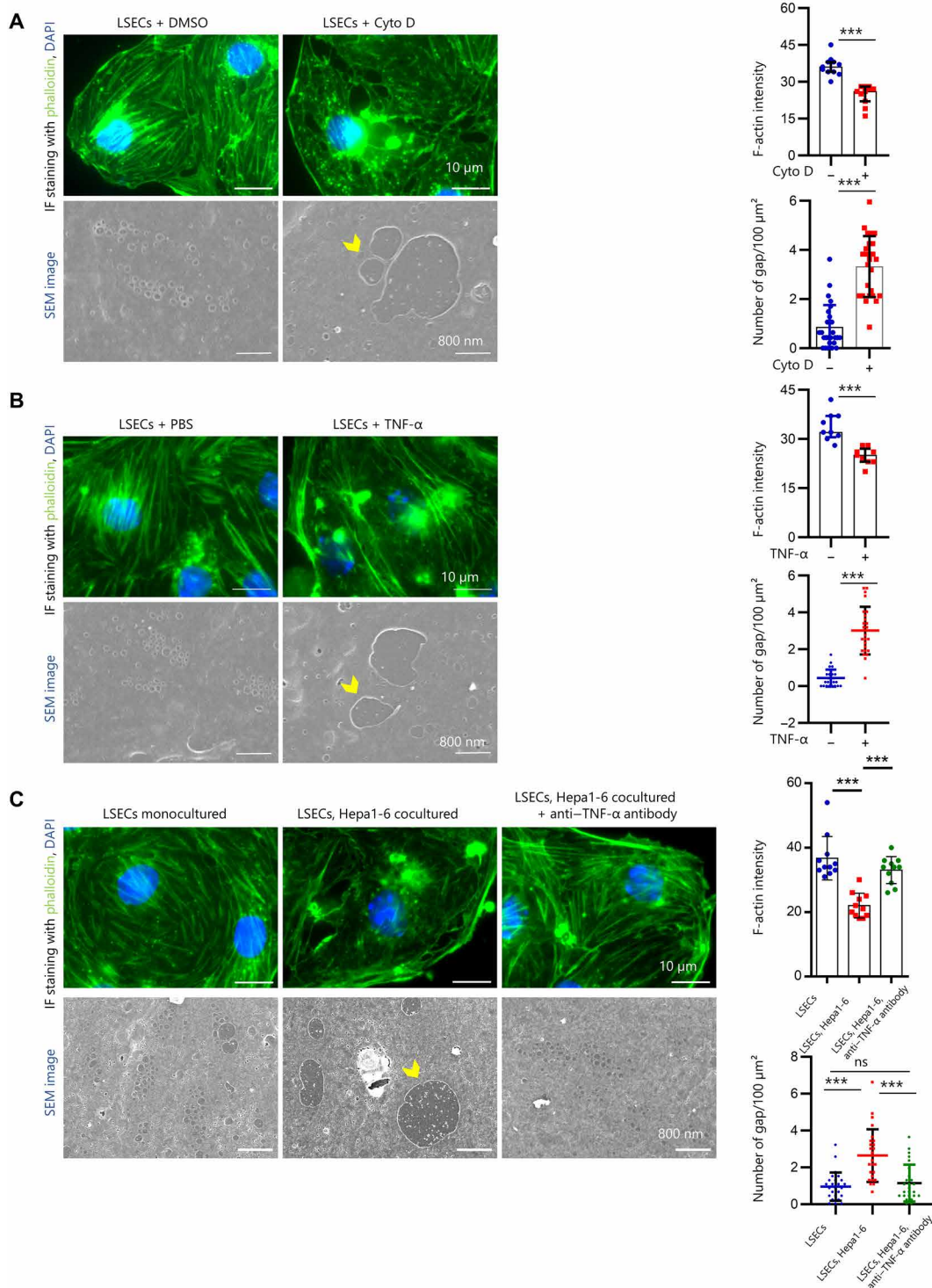


Fig. 5. Dynamic actin disassembly is caused by TNF- α . (A to C) Representative phalloidin (green) and DAPI (blue) staining, corresponding SEM images, and the quantification of F-actin fluorescence; number of LSECs-iGap in LSECs of: (A) LSECs treated with dimethyl sulfoxide (DMSO) (control) and 1 μ M CytoD for 24 hours, (B) LSECs treated with phosphate-buffered saline (PBS) (control) and rmTNF- α (50 ng/ml) for 24 hours, and (C) monocultured LSECs and LSECs cocultured with Hepa1-6 cells with or without mouse TNF- α -neutralizing antibody (100 ng/ml) for 24 hours. Scale bar in phalloidin staining and SEM images are 10 μ m and 800 nm, respectively. Quantitation of F-actin fluorescence intensity per area. Data were quantified from at least 150 cells, $N = 3$ for each group. Data are shown as means \pm SD. *** $P < 0.001$, two-tailed unpaired Student's t test (A and B) and one-way ANOVA (C). The yellow arrowhead indicated the LSECs-iGap. Scale bar, 10 μ m in IF staining images and 800 nm in SEM images.

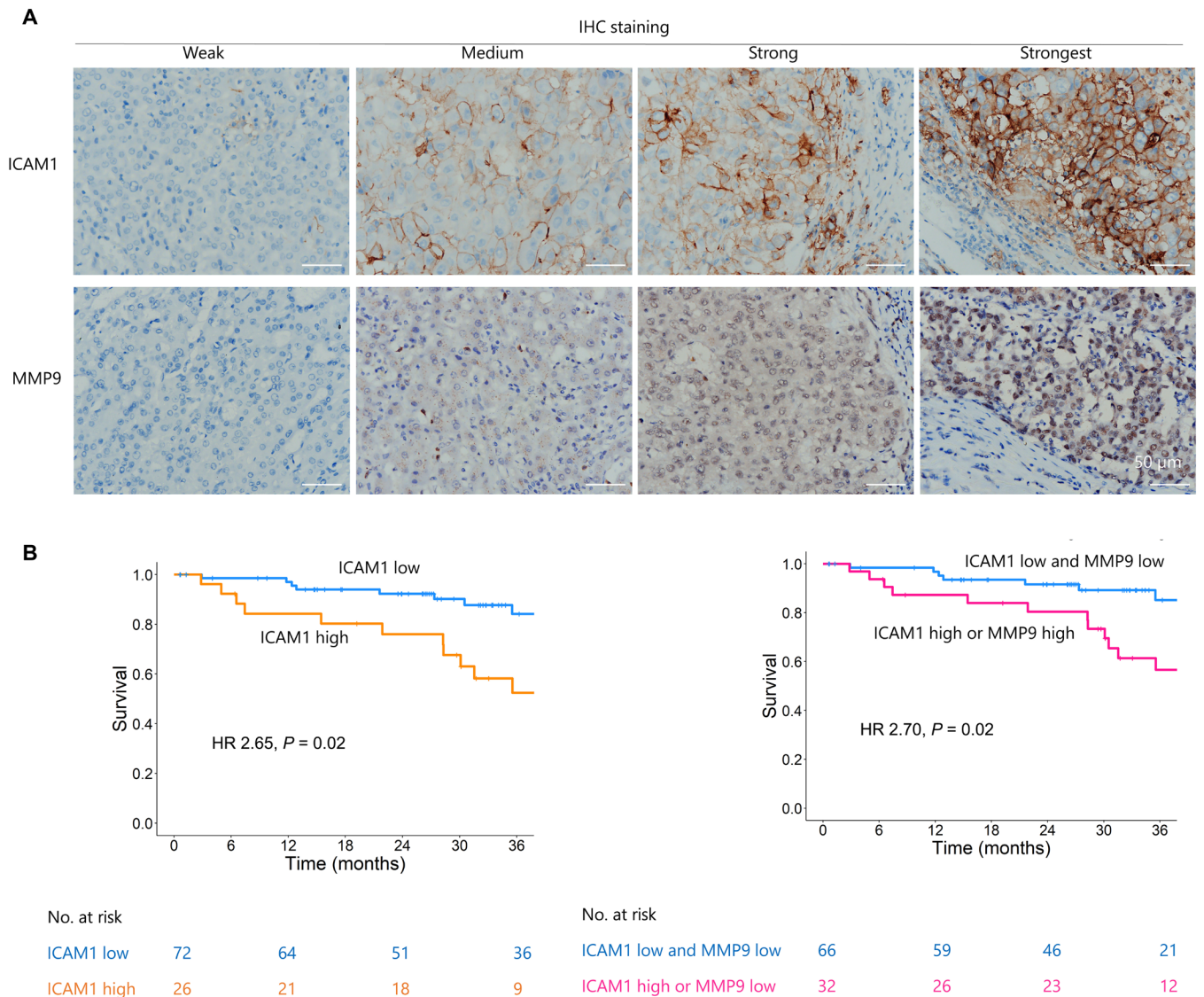


Fig. 6. MMP9 and ICAM1 were associated with intrahepatic metastasis and survival outcomes in patients with HCC. (A) Representative images of ICAM1 and MMP9 staining in HCC specimens with different grades of staining intensity (weak, medium, strong, and strongest). Scale bar, 50 μm . **(B)** Kaplan-Meier curves show the association between low and high levels of ICAM1 and MMP9 staining and overall survival time (more details in the Supplementary Materials). HR, hazard ratio.

disruption of endothelial cell-cell junctions (8, 32). In rare cases in vitro, tumor cells cross the endothelium by infiltrating individual cell bodies in a process termed transcellular migration (33). In the present study, we demonstrated in vivo and in vitro that Hepa1-6 cells protruded into and then broke through LSECs-iGap to infiltrate the liver parenchyma. These LSECs-iGap resulted from both hepatotoxin administration and early-stage interactions with Hepa1-6 cells. It is probable that cancer cells induce LSECs-iGap by opening the fenestra-like “door” and facilitating entry into the liver parenchyma. We confirmed this process using several mouse models, showing that the number of LSECs-iGap was positively correlated with that of metastatic foci. Furthermore, we found that the effect of Hepa1-6 cells on LSECs differed from that of primary mouse hepatocytes, suggesting that interaction with cancer cells is an important process for downstream signaling involved in LSECs-iGap formation. It was previously reported that such a phenomenon

occurs in some mouse models after discontinuation of anti-vascular endothelial growth factor treatment (12). Furthermore, circulating tumor cells, which are frequently observed in the peripheral blood of patients with advanced cancer (34, 35), have been reported to increase in number after chemotherapy (19).

Many antineoplastic drugs, such as cyclophosphamide, oxaliplatin, and 6-MP (6-mercaptopurine), can cause blockage of the central and sublobular veins of the liver, resulting in SOS, which was previously termed veno-occlusive disease (36–38). In SOS, LSECs that develop iGap are thought to contribute to hemorrhage. In mouse models, we observed chemically induced and fibrosis-induced iGap up to 3 μm in diameter in LSECs. Hepa1-6 cells injected into the spleens of mice appeared in the lumen of the liver and transmigrated to the liver tissue via LSECs-iGap. This liver infiltration was confirmed by the appearance of tumor foci in the liver 3 to 5 days later. Joseph *et al.* (39) reported that MCT promoted transplant cell engraftment,

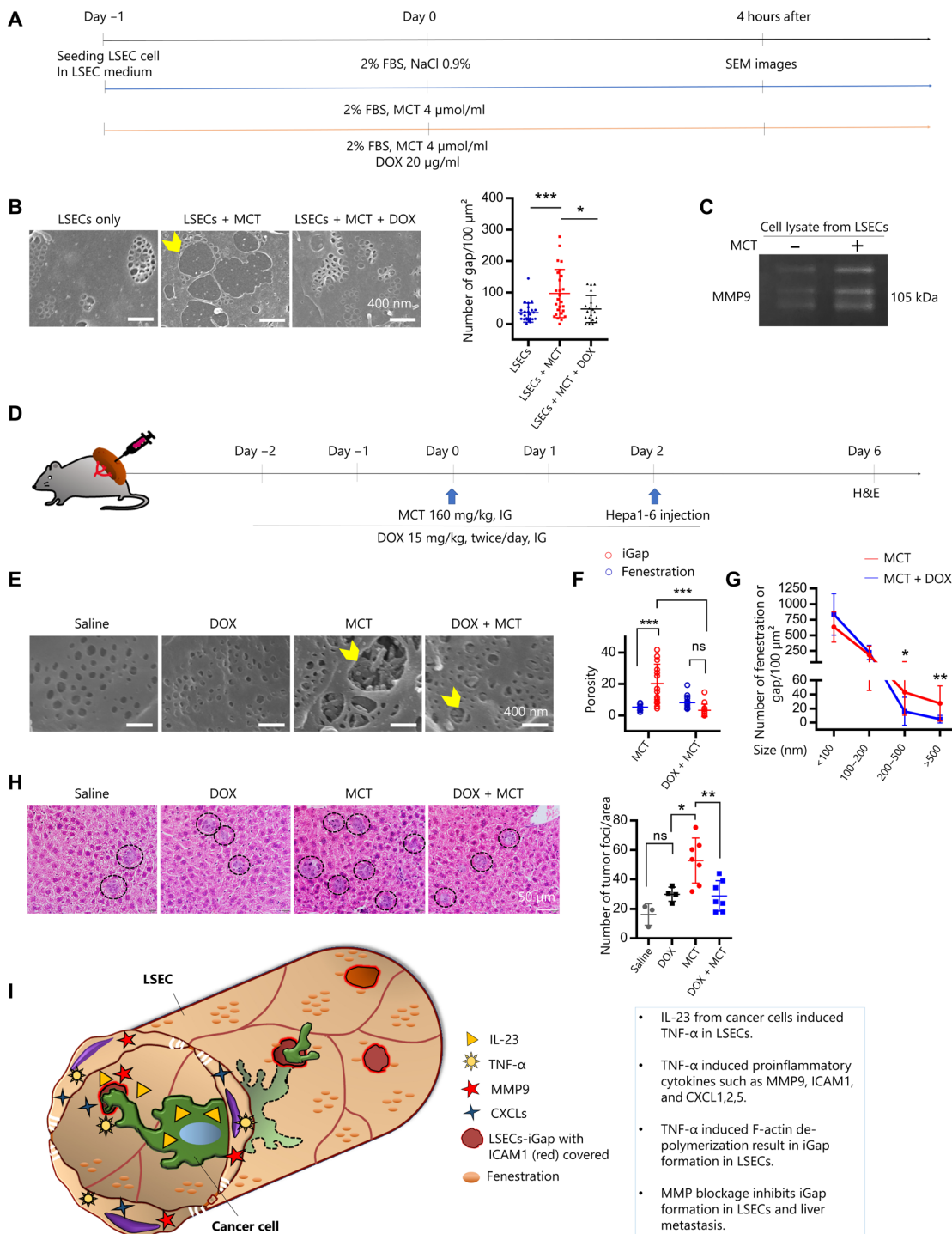


Fig. 7. MMP inhibition reduces LSECs-iGap and attenuates liver metastasis. (A) A schematic diagram of the treatment of LSECs with MCT (4 $\mu\text{mol/ml}$) with or without DOX (20 $\mu\text{g/ml}$) for 4 hours. FBS, fetal bovine serum. (B) Representative SEM images of LSECs-iGap (yellow arrowhead) after 4 hours of MCT treatment and quantitation of the average number of LSECs-iGap per 100 μm^2 . Scale bar, 400 nm. (C) Gelatin zymography to detect MMP9 activity in LSECs (cell lysates) after 4 hours of MCT treatment. (D) Schematic of the mouse model of liver metastasis using intrasplenic injection of Hepa1-6 cells after pretreatment with MCT alone or in combination with DOX. IG, intragastric. (E) Representative SEM images of LSECs-iGap in liver sinusoid (yellow arrowheads) on day 2 after saline (control), DOX, MCT, or DOX/MCT treatment. Scale bar, 400 nm. (F) The average number of LSECs-iGap per 100 μm^2 with different diameters after MCT treatment with or without DOX pretreatment. (G) Quantification of the porosity of fenestration and LSECs-iGap after MCT and DOX treatments. (H) Representative H&E staining of tumor foci in the liver (black circles) 3 days after intra-splenic injection of Hepa1-6 cells and quantitation of the average number of tumor foci per unit area. Scale bar, 50 μm . (I) Diagram of cancer cell invading through LSECs-iGap. Data were quantified from $n = 3$ to 7 mice in each group as described above. The average number of LSECs-iGap was quantified from at least 25 random fields, $N = 3$ per group. Data are shown as means \pm SD. * $P < 0.05$, ** $P < 0.01$, and *** $P < 0.001$, one-way ANOVA.

presumably using a similar mechanism. Furthermore, although surgical sections of HCC properly fixed for SEM analysis were not readily available, specimens of biopsy-diagnosed liver fibrosis showed the appearance of iGap in human LSECs. Moreover, LSECs-iGap were more likely to appear in nonfibrotic areas adjacent to fibrotic areas, where capillarization occurs. This observation is consistent with a previous study showing the appearance of LSECs-iGap in human samples (11). In addition, a retrospective analysis of colorectal cancer showed that hepatic fibrosis significantly promoted liver metastasis (40). These data suggest that the fibrotic milieu or at least a dedifferentiated sinusoidal endothelium in the liver influences the ability of cancer cells to metastasize to the liver, with LSECs-iGap being an important factor. This unique characteristic of LSECs profoundly contributes to our understanding of how cancer cells metastasize to the liver. However, it is still necessary to clarify whether LSECs-iGap formation is unique to LSECs or also occurs in endothelial cells of other organs.

The activation of MMP family proteins, primarily MMP2 and MMP9, has been reported to be involved in LSECs-iGap induced by hepatotoxins such as APAP (27), galactosamine/endotoxin, and galactosamine/TNF- α (25). MMP2 and MMP9 are the major gelatinases (41). Among the MMPs, only MMP9 expression was induced in LSECs cocultured with Hepa1-6 cells in our study. Hepa1-6 cell transmigration was significantly suppressed in shMMP9-LSECs compared with that in control LSECs, suggesting that the activity of MMP9, but not MMP2, uniquely participates in LSECs-iGap formation induced by the interaction of LSECs with cancer cells. Recent studies showed the distinct role of MMP2 and MMP9 in tumor angiogenesis and metastasis; using urokinase plasminogen/MMP2/MMP9 transgenic and knockout mice and pharmacological inhibitors, MMP9, but not MMP2, was shown to be produced from the tumor microenvironment and to contribute to the initiation of tumor angiogenesis (42). Moreover, similar to our results, high expression of MMP9 was shown to be a possible prognostic factor for poor outcomes in many cancers, including HCC (43, 44). Notably, we demonstrated that the invasion and metastatic potential of Hepa1-6 cells were significantly attenuated by suppression of LSECs-iGap formation by MMP inhibition. This result strongly supports MMP9 as a potential therapeutic target to prevent cancer metastasis.

Using a cytokine array to search for causative factors that control LSECs-iGap formation, we found that Hepa1-6 cells specifically expressed IL-23 in the medium under coculture conditions with LSECs. Although the function of IL-23 is not fully understood, previous studies showed that increased IL-23 expression was associated with cancer metastases via up-regulation of proangiogenic and proinflammatory factors (45). In coculture conditions, all factors detected in the medium, except IL-23, were derived from LSECs and not from Hepa1-6 cells. Because treatment with rmIL-23 induced TNF- α proteins in a dose-dependent manner in medium from cultured LSECs, we concluded that IL-23 acts upstream of TNF- α . TNF- α is an inflammatory cytokine that acts at sites of vascular injury and regulates vascular smooth muscle cells and endothelial cells by transmitting signals involved in proliferation, differentiation, and apoptosis (46). We found that TNF- α expression by LSECs triggered a series of proinflammatory responses and expression of downstream genes including MMP9, ICAM1, CXCL1, CXCL2, and CCL5.

We also demonstrated that F-actin depolymerization accompanied LSECs-iGap formation and that TNF- α is an F-actin modulator. This evidence might explain previous findings in other hepatotoxic

mouse models, where LSECs-iGap appeared in the liver treated with APAP (47) or MCT (48), as these models also showed increased levels of TNF- α in the peripheral blood, similarly to an increase in TNF- α observed in the APAP-treated liver. TNF- α was previously reported to depolymerize F-actin to monomeric G-actin in pulmonary vascular endothelial cells (49), yet the mechanism remains unclear. Further study is therefore needed to clarify the function of TNF- α during formation of LSECs-iGap.

Among the TNF- α downstream signaling pathways, ICAM1 appeared to be involved in the interaction of Hepa1-6 cells with LSECs by being selectively expressed at the edge of LSECs-iGap. ICAM1 is a key cell surface glycoprotein for cellular adhesion that is widely expressed in many cell types, including endothelial cells and inflammatory cells (50). Expression of ICAM1 is up-regulated in response to various inflammatory mediators, including TNF- α (51). Furthermore, elevated levels of ICAM1 have been reported in many malignancies (52, 53) and in liver metastasis (28). We found that ICAM1 silencing in LSEC monolayers reduced Hepa1-6 cell adhesion and transmigration. ICAM1 is expressed in both LSECs and cancer cells, leading to adhesion of cancer cells to LSECs in the early stages of liver metastasis (28). Together with high expression of MMP9, high expression of ICAM1 in LSECs and cancer cells was correlated with poor prognoses in our clinical cohort.

In summary, our findings identified a key role of LSECs-iGap formation in liver metastasis, which is induced by the interaction between LSECs and Hepa1-6 cells. The secretion of IL-23 by Hepa1-6 cells causes TNF- α production in LSECs, which in turn propagates actin disassembly and induced downstream MMP9 and ICAM1 expression in LSECs. Our findings provide a novel concept for cancer metastasis to the liver and contributes to the development of new therapies for preventing metastatic cancers by targeting LSECs-iGap formation.

MATERIALS AND METHODS

Clinical sample collection

Formalin-fixed and paraffin-embedded tissue samples were obtained from 98 patients with HCC who underwent surgical resection at Osaka City University Hospital (currently named Osaka Metropolitan University Hospital) (Osaka, Japan). The guidelines of the Liver Cancer Study Group of Japan (54) were used to evaluate the histological classification of the tumors and the status of the background liver tissues. The tumors were graded histologically and differentiated, moderately differentiated, or poorly differentiated. Clinical and pathological reports were reviewed for clinical features including demographic data (age and sex), number of tumors, tumor size, overall survival, vascular invasion, and recurrence (see the Supplementary Materials for more details). The study was approved by the ethics committee of Osaka City University (currently named Osaka Metropolitan University) and was in compliance with the Helsinki Declaration (Ethic No. 2021-200). All patients provided written informed consent before tissue samples were obtained.

Cancer cell lines

All in vitro and in vivo experiments were conducted using the Hepa1-6 hepatoma cell line derived from C57L mice (American Type Culture Collection CRL-1830), the Colon26 colon cancer cell line derived from BALB/c mice (Riken BRC, Tokyo, Japan), and the 4T1 breast cancer cell line provided by L. M. Wakefield from the Center for Cancer Research, National Cancer Institute [National Institutes of

Health (NIH), Bethesda, MD, USA] (55). The human HCC line HepG2 (JCRB1054) was obtained from the Health Science Research Resources Bank (Osaka, Japan) (56). Cancer cells were cultured in complete DMEM (DMEM low glucose; Gibco, Thermo Fisher Scientific, Waltham, MA, USA) consisting of 10% fetal bovine serum (FBS; Hyclone, Cytiva, London, UK) and 1% penicillin-streptomycin (P/S; Fujifilm Wako Pure Chemical Corporation, Osaka, Japan) [DF-10 (10% FBS/DMEM)] in a humidified atmosphere containing 95% air and 5% CO₂ at 37°C.

Animals

Male C57/BL6J mice 6 to 8 weeks of age were purchased from Japan SLC Inc. (Shizuoka, Japan). All mice received humane care in accordance with the Guide for the Care and Use of Laboratory Animals. All protocols and experimental procedures were approved by the Institutional Animal Care and Use Committee of Osaka City University (currently named Osaka Metropolitan University) and performed following NIH guidelines for the use of animals in research. Mice were housed in a temperature-controlled (24° ± 1°C) environment with 55 ± 5% humidity and alternating 12-hour light/12-hour dark cycles. The mice had free access to water and a standard rodent diet.

Reagents and materials

In vivo, CL (Macrokiller reagent, Cosmo Bio, Tokyo, Japan) was injected intraperitoneally. The next day, Hepa1-6 cells were intrasplenically injected. Mice were injected intraperitoneally with MMP2/9 inhibitor {*N*-[(1,1'-biphenyl)-4-ylsulfonyl]-*D*-phenylalanine, Abcam, Cambridge, UK} 1 day before injection of cells (day -1). The next day (day 0), Hepa1-6 cells (2 × 10⁶ cells) were intrasplenically injected 30 min after another injection of MMP2/9 inhibitor (2.5 mg/kg of body weight). Resulting tumor foci were observed on day 3.

In vitro, primary LSECs (6 × 10⁵) were seeded on 12-well plates in LSEC medium. The next day, the medium was changed to DF-0.2, and the cells were treated with rmTNF-α (R&D Systems, Minneapolis, MN, USA) and IL-23 (R&D Systems) for 24 hours at final concentrations of 10 and 25 ng/ml, respectively. Anti-mouse TNF-α-neutralizing antibody (Cell Signaling Technology, Beverly, MA, USA) was used at a concentration of 100 ng/ml for 24-hour treatment. CytoD was purchased from Wako Fujifilm. Cells were pretreated with CytoD at 1 μM for 30 min, washed three times with DMEM, and cultured using DF-0.2 for 24 hours. MCT (4 μmol/ml, Fujifilm Wako) was used to treat LSECs for 4 hours.

APAP mouse model

Mice were divided into two groups of six mice each. The treated group was injected intraperitoneally with APAP (Sigma-Aldrich, St. Louis, MO, USA) at a dose of 300 mg/kg body weight, whereas the control group was injected with 0.9% NaCl. After 6 hours, three mice of each group were euthanized, and their liver sinusoids were observed by SEM. The remaining mice were intrasplenically injected with 2 × 10⁶ Hepa1-6 cells, and their spleens were removed 5 min after the injection. Three days after Hepa1-6 cell injection, H&E staining was conducted to analyze the number of hepatic metastases.

Mouse model of liver fibrosis using TAA

Male C57/BL6J mice at 12 weeks of age were given intraperitoneal injections of escalating doses of TAA (Fujifilm Wako). The first dose was 50 mg/kg body weight, and the second dose was 100 mg/kg. The mice were then sequentially administered TAA (200, 300, and

400 mg/kg) twice weekly for 2 to 3, 4 to 5, and 6 to 12 weeks, respectively. Three days after the last TAA injection, Hepa1-6 cells were injected into the spleens of the mice. The liver sinusoid was examined by SEM, and the number of liver metastases was analyzed using H&E and Sirius Red staining.

SEM and TEM analyses

The fixation solution consisted of 2.5% glutaraldehyde (TAAB laboratories equipment Ltd., Berks, UK), 2% paraformaldehyde, and 50% 0.2 M sodium cacodylate buffer. To prepare in vitro samples, LSECs were seeded on 12-mm micro cover glass (Matsunami Glass Ind. Ltd., Osaka, Japan) and then fixed overnight at 4°C with the fixation solution. For in vivo experiments, mice were anesthetized with parapentobarbital (6.48 mg/ml; Somnopentyl, Kyoritsu Seiyaku, Tokyo, Japan) and subsequently perfused with fixation solution at a rate of 1 ml/min for 5 min (57). The liver was then dissected to about 2-mm thickness and immersed in fixation solution at 4°C overnight. The next day, the liver tissues were sliced into 300-μm-thick sections using a microtome (Neo LinearSlicer MT, Dosaka-Em, Kyoto, Japan). The fixed cells on the cover glass or the 300-μm sectioned tissues were then washed three times for 20 min with sodium cacodylate buffer solution (pH 7.4) (Fujifilm Wako). The specimens were postfixed with 2% osmium (VIII) oxide solution (OsO₄; Fujifilm Wako), dehydrated with a stepwise ethanol gradient (50, 70, 80, 90, and 100%), and lastly immersed in 100% ethanol at room temperature overnight. Next, the specimens were immersed in isopropyl alcohol (Fujifilm Wako) for 20 min and then dried using a critical point dryer (HCP-2; Hitachi, Tokyo, Japan) with carbon dioxide. After drying, the specimens were mounted on an aluminium stub and coated with platinum (E-1030, Hitachi). The tissue specimens were analyzed using an ultra-field emission scanning electron microscope (S-4700SI; Hitachi) at 30 kV.

For TEM processing, postfixation was performed with 2.0% OsO₄ in phosphate buffer for 90 min on ice, and small specimens were dehydrated and embedded in a Quetol 812 mixture (Nissin-EM, Tokyo, Japan). Ultrathin sections of 70-nm thickness were cut using an ultramicrotome (Ultracut UCT; Leica, Wetzlar, Germany) and stained with 2% uranyl acetate and lead citrate solutions. The ultrathin sections were observed using a TEM instrument (Talos F200; FEI, Cambridge, UK) at an accelerating voltage of 200 kV. Images were analyzed using ImageJ software (<http://rsb.info.nih.gov/ij/>). The number of LSECs-iGap (with a diameter of more than 250 nm) was counted in each area of the LSECs. For each experiment, at least eight random images were analyzed per sample, and a total of at least 25 images were analyzed per group. The total count of gap formations per image was also normalized to the area to give the gaps/100 μm². Porosity of fenestrae and iGap were determined according to a procedure described previously, as a ratio of the area occupied by the fenestrae and iGap to the total area where they could be formed.

Three-dimensional tomography reconstruction

Ultrathin serial sections of 200-nm thickness were cut using an ultramicrotome and stained with 2% uranyl acetate solution and lead citrate solution. The ultrathin serial sections were then coated with carbon and observed by SEM at an accelerating voltage of 3.0 kV. The resultant image stack and reconstruction of the 3D structure were processed using ImageJ (NIH), Microscopy Image Browser (University of Helsinki, Helsinki, Finland), and Amira2019 (Thermo Fisher Scientific).

Primary mouse LSECs, hepatocyte isolation, and human endothelial cells

Primary mouse LSECs and hepatocytes were isolated in our laboratory from C57BL/6J mice using a modified version of a previously published protocol (58). The detailed protocol is described in the Supplementary Materials (Methods; “Primary mouse LSECs and hepatocyte isolation” section). LSECs were cultured in the EGM-2 MV Microvascular Endothelial Cell Growth Medium-2 SingleQuots Kit (LSEC medium; Lonza, Basel, Switzerland), and hepatocytes were maintained in DF-10. HUVECs were obtained from Lonza and maintained in LSEC medium.

LSECs cocultured with Hepa1-6 cells and hepatocytes

Freshly isolated primary LSECs were seeded at the bottom of the wells of a six-well insert plate (Corning Falcon, Glendale, AZ, USA) in LSEC medium. Hepa1-6 cells and primary mouse hepatocytes were separately seeded on 3- μ m pore size inserts (Corning, Falcon) in DF-10. After 18 hours, the media for all cell types were removed, the cells were washed three times with DMEM, and new medium consisting of 2% FBS, DMEM low glucose, and 1% antibiotic (DF-2) was added. The inserts seeded with hepatocytes or Hepa1-6 cells were then placed in the wells with the LSECs. After 24 hours of coculture, the cells were separately harvested and analyzed.

DOX treatment in vitro

Isolated primary LSECs were seeded at the bottom of the wells of a 24-well plate (Corning, Falcon) in LSEC medium. Hepa1-6 cells were then seeded on inserts as described above. The next day, the LSECs were treated with DF-2 supplemented with or without DOX (20 μ g/ml; Fujifilm Wako) for 2 hours and then washed three times with DMEM. The inserts containing Hepa1-6 cells were then placed into the wells on top of the LSECs. After 16 hours of coculture, all cells were fixed with SEM fixative for electron microscopy analysis.

RNA-seq and data analysis

RNA-seq was performed on LSECs and Hepa1-6s in monoculture or coculture ($n = 3$ each group). RNA was extracted using TRIzol reagent (Thermo Fisher Scientific) and purified using the Direct-zol RNA Miniprep (Zymo Research, Irvine, CA, USA) according to the manufacturer’s protocol. The resulting mRNA was fragmented and reverse-transcribed using random primers into complementary DNA (cDNA). Adapters were ligated onto both ends of the cDNA fragments. The RNA libraries were then sequenced using the NovaSeq 6000 platform (Macrogen, Seoul, Korea). Quality control of the sequenced raw reads was performed using the sequencing control software, FastQC v0.11.7. Trimmed reads were mapped to the reference genome with HISAT2, and then transcripts were assembled using StringTie with the aligned reads. Expression profiles are represented as read counts, and normalization values are based on the transcript length and coverage depth. The FPKM value or the reads per kilobase of transcript per million mapped reads was used as the normalization value. The multivariate analysis for PLS-DA was carried out using SIMCA® Multivariate Data Analysis software (Umetrics, Umea, Sweden) in the R stat package. The Enricher web tool was used to find the pathways and GO terms shared from the Oncomine database (<https://amp.pharm.mssm.edu/Enrichr>). The enriched GO terms and pathways were visualized as a bar diagram (Fig. 4A and fig. S4A). Statistical analysis was performed using fold changes with the independent t test for each comparison

pair. Significant results were selected on the conditions of $|fc| \geq 2$ and independent t test raw P value of <0.05 .

Zymography assay

Conditioned media collected from LSECs and Hepa1-6 cells in monoculture, direct coculture, or indirect coculture using inserts were concentrated using an Amicon Ultra centrifugal filter unit with a membrane pore size of 10 kDa (Merck Millipore, Burlington, MA, USA) to 100 μ l of final volume. Then, 7.5 μ l of concentrated medium was loaded on a gelatinase gel. To obtain cell lysates or tissue lysates from LSECs or mouse liver specimens, we used lysis buffer consisting of 25 mM tris-HCl (pH 7.5), 100 mM NaCl, and 1% Nonidet P-40 (NP-40). The protease inhibitor was added to a 1% final concentration before use. After the protein concentration was measured, the amounts of loading protein from cell and tissue lysates were 3 and 10 μ g, respectively. The samples were run on gelatinase gel (Invitrogen Thermo Fisher Scientific), washed in renaturing buffer (Novex Thermo Fisher Scientific, Waltham, MA, USA), and incubated with developing buffer (Novex Thermo Fisher Scientific) for 24 hours. The gel was then stained with Coomassie Brilliant Blue solution for 1 hour and washed with washing solution consisting of 10% acetic acid and 10% methanol in distilled water until visually clear (59).

Cytokine screening

Mouse cytokine profiling was performed using a Proteome Profiler Mouse XL Cytokine Array Kit (R&D Systems, Minneapolis, MN, USA), which detects 111 soluble mouse cytokines. First, 3.5×10^5 primary LSECs were seeded into each well of a 24-well plate immediately after isolation in LSEC medium. The next day, the medium was removed, and the cells were washed three times with DMEM solution. Then, 7×10^4 Hepa1-6 cells suspended in 500 μ l of DF-0.2 solution were added to the coculture group, whereas 250 μ l of DF-0.2 solution was added to the LSEC monoculture group. At the same time, 7×10^4 Hepa1-6 cells suspended in 250 μ l of DF-0.2 solution were placed into other wells as Hepa1-6 monocultures. After 24 hours, the conditioned medium from the coculture group and the combined media from the LSECs and Hepa1-6 cell monocultures were collected. Mouse XL Cytokine Arrays were incubated overnight at 4°C with 600 μ l of the cell culture supernatants, and the screening procedure was performed according to the manufacturer’s instructions (Supplementary Materials, Methods; “Cytokine array” section).

Lentiviral shRNA and T.E.M. for LSECs

ICAM1 and MMP9 knockdown plasmids pLKO.1-shICAM1 and pLKO.1-shMMP9 (reference sequence numbers NM_010493 and NM_013599, respectively) along with the control plasmid pLKO.1-shGFP were purchased from Sigma-Aldrich-SHCLNG (06242112MN and 06242110MN; Sigma-Aldrich). The lentivirus package plasmids pCMV-VSV-G and psPAX2 were purchased from Addgene (Watertown, MA, USA). Cell transfection was performed using a transfection reagent according to the manufacturer’s instructions. The pLKO.1-shICAM1, pLKO.1-shMMP9, or pLKO.1-shGFP plasmids were cotransfected along with the pCMV-VSV-G and psPAX2 plasmids into 293T cells to produce lentiviral particles. The culture medium was collected and exchanged for fresh medium every day. LSECs with stable ICAM1 or MMP9 knockdown and control primary LSECs were generated 2 days after infection with the lentiviral particles.

First, 2×10^5 LSECs were seeded onto inserts with 8- μ m pore size inserts (Corning Falcon) in LSEC medium on 24-well Transwell plates. The next day, the medium was removed, and the inserts were washed three times with DMEM solution. Then, medium containing GFP, ICAM1, or MMP9 shRNA lentivirus was added, and the transwell plates were incubated at 37°C for 48 hours. LSECs with shGFP served as the control group. The medium was removed, and the insert was washed three times with DMEM. Then, 250 μ l of FBS-free DMEM with 1×10^4 Hepa1-6 cells were transferred into the transwell plates with the inserts containing LSECs, and 250 μ l of DF-10 was added into the lower chambers of the wells. After the cultures were incubated at 37°C for 24 hours, the cells on the top side of the transwell membrane were removed, and those that migrated to the bottom side of the membrane were examined using a microscope (Olympus, Tokyo, Japan) after being stained with crystal violet. Ten images were taken randomly at different locations for each membrane. Each step of the T.E.M. was carefully performed by microscopic observation and was repeated thrice.

IHC of HCC tissues

Surgically dissected tissue specimens from patients with HCC were deparaffinized with xylene, rehydrated using graded alcohols, and pressure-cooked for 3 min in citrate buffer (pH 6.0) for antigen retrieval. The slides were then washed with phosphate-buffered saline (PBS) and treated with 3% hydrogen peroxide for 20 min to quench endogenous peroxidase activity. Then, the samples were preincubated with 10% goat serum at room temperature for 30 min to prevent nonspecific staining. In addition, the cancerous foci and nontumorous samples were incubated with rabbit polyclonal anti-ICAM1 antibody (1:200 dilution; BioVision, Milpitas, CA, USA) overnight in a humidified container at 4°C. The next day, the slides were washed with PBS, treated with a biotinylated horseradish peroxidase detection system according to the manufacturer's instructions, and stained with 3,3'-diaminobenzidine tetrahydrochloride. Last, the sections were counterstained with Mayer's hematoxylin, dehydrated, and mounted. The primary antibody was replaced with normal goat serum to obtain a negative control. Staining intensity and the percentage of immunoreactive cells over total tumor cells were considered throughout the evaluation process. No interobserver variability was accepted. The stained tissue sections for ICAM1 and MMP9 were assessed using a four-point scale by percentage of positive staining per field as follows: A score of 1 was assigned if $\leq 3.4\%$, $\leq 1\%$ of cells were stained; score 2 if 3.5 to 6.8%, 1 to 2% of cells were immunoreactive; score 3 if 6.9 to 10.2%, 3 to 4% of cells were immunoreactive; and score 4 if $\geq 10.3\%$, $\geq 5\%$ of cells were immunoreactive.

MCT and DOX treatments for in vivo experiments

Mice received a single intragastric dose of 160 mg/kg body weight MCT on day 0 or an equivalent volume of vehicle (saline) for control. To inhibit MMP activity, 15 mg/kg body weight DOX was given intragastrically twice daily from day -2 until day 1 of the experiment (Fig. 6A). To access SEM images of fenestration and/or LSECs-iGap, we observed three mice in each treatment group on day 2. To analyze hepatic metastasis, we injected 2×10^6 Hepa1-6 cells into the spleen and measured the results after 5 days using H&E staining.

Statistical analysis

All experiments were replicated at least three times. ImageJ (NIH) was used to evaluate the band intensities for Western blot analyses.

The data presented as bar graphs are the means \pm SD in all experiments. Statistical analyses were performed using Student's *t* test (two-tailed) or analysis of variance (ANOVA) with multiple comparisons using one-way ANOVA. Significant differences among groups are indicated as **P* < 0.05, ***P* < 0.01, and ****P* < 0.001.

Baseline characteristics of the patients were analyzed using the chi-square test for categorical variables and Mann-Whitney *U* test for continuous variables. Univariate and multivariate logistic regression were used to assess associations in patients with or without vascular invasion. The cumulative survival probability was estimated using the Kaplan-Meier method and HR (hazard ratio) based on univariate and multivariate Cox regression. The albumin-bilirubin score was calculated using serum albumin and total bilirubin levels [\log_{10} bilirubin (μ M) \times 0.66] + (albumin in g/liter) \times -0.08 5], which assessed liver function in HCC (60). All analyses of human data were performed using R statistical software, version 3.6.0 (The R Foundation for Statistical Computing, Vienna, Austria). All reported *P* values were two-sided, with *P* values of <0.05 considered statistically significant.

SUPPLEMENTARY MATERIALS

Supplementary material for this article is available at <https://science.org/doi/10.1126/sciadv.abo5525>

[View/request a protocol for this paper from Bio-protocol.](#)

REFERENCES AND NOTES

1. T. Bogenrieder, M. Herlyn, Axis of evil: Molecular mechanisms of cancer metastasis. *Oncogene* **22**, 6524–6536 (2003).
2. K. R. Hess, G. R. Varadhachary, S. H. Taylor, W. Wei, M. N. Raber, R. Lenzi, J. L. Abbruzzese, Metastatic patterns in adenocarcinoma. *Cancer* **106**, 1624–1633 (2006).
3. M. Mitsunobu, A. Toyosaka, T. Oriyama, E. Okamoto, N. Nakao, Intrahepatic metastases in hepatocellular carcinoma: The role of the portal vein as an efferent vessel. *Clin. Exp. Metastasis* **14**, 520–529 (1996).
4. F. Vidal-Vanaclocha, The prometastatic microenvironment of the liver. *Cancer Microenviron.* **1**, 113–129 (2008).
5. N. N. Khodarev, J. Yu, E. Labay, T. Darga, C. K. Brown, H. J. Maurer, R. Yassari, N. Gupta, R. R. Weichselbaum, Tumour-endothelium interactions in co-culture: Coordinated changes of gene expression profiles and phenotypic properties of endothelial cells. *J. Cell Sci.* **116**, 1013–1022 (2003).
6. O. I. Hoffmann, C. Ilmberger, S. Magosch, M. Joka, K. W. Jauch, B. Mayer, Impact of the spheroid model complexity on drug response. *J. Biotechnol.* **205**, 14–23 (2015).
7. M. K. Connolly, A. S. Bedrosian, A. Malhotra, J. R. Henning, J. Ibrahim, V. Vera, N. E. Cieza-Rubio, B. U. Hassan, H. L. Pachter, S. Cohen, A. B. Frey, G. Miller, In hepatic fibrosis, liver sinusoidal endothelial cells acquire enhanced immunogenicity. *J. Immunol.* **185**, 2200–2208 (2010).
8. D. Schumacher, B. Strilic, K. K. Sivaraj, N. Wettschreck, S. Offermanns, Platelet-derived nucleotides promote tumor-cell transendothelial migration and metastasis via P2Y₂ receptor. *Cancer Cell* **24**, 130–137 (2013).
9. J. W. Sturm, R. Magdeburg, K. Berger, B. Petrich, S. Samel, R. Bönninghoff, M. Keese, M. Hafner, S. Post, Influence of TNFA on the formation of liver metastases in a syngenic mouse model. *Int. J. Cancer* **107**, 11–21 (2003).
10. S. A. Wohlfel, V. Häfele, B. Dietsch, K. Schledzewski, M. Winkler, J. Zierow, T. Leibing, M. M. Mohammadi, J. Heineke, C. Sticht, V. Olsavszky, P. S. Koch, C. Gérard, S. Goerdert, Hepatic endothelial notch activation protects against liver metastasis by regulating endothelial-tumor cell adhesion independent of angiocrine signaling. *Cancer Res.* **79**, 598–610 (2019).
11. F. Braet, E. Wisse, Structural and functional aspects of liver sinusoidal endothelial cell fenestrae: A review. *Comp. Hepatol.* **1**, 1 (2002).
12. E. Wisse, R. B. De Zanger, K. Charels, P. Van Der Smissen, R. S. McCuskey, The liver sieve: Considerations concerning the structure and function of endothelial fenestrae, the sinusoidal wall and the space of Disse. *Hepatology* **5**, 683–692 (1985).
13. N. A. Hutchins, F. Wang, Y. Wang, C. S. Chung, A. Ayala, Kupffer cells potentiate liver sinusoidal endothelial cell injury in sepsis by ligating programmed cell death ligand-1. *J. Leukoc. Biol.* **94**, 963–970 (2013).
14. Y. Fukuda, H. Nagura, M. Imoto, Y. Koyama, Immunohistochemical studies on structural changes of the hepatic lobules in chronic liver diseases. *Am. J. Gastroenterol.* **81**, 1149–1155 (1986).

15. J. Gracia-Sancho, E. Caparrós, A. Fernández-Iglesias, R. Francés, Role of liver sinusoidal endothelial cells in liver diseases. *Nat. Rev. Gastroenterol. Hepatol.* **18**, 411–431 (2021).
16. L. D. DeLeve, Liver sinusoidal endothelial cells in hepatic fibrosis. *Hepatology* **61**, 1740–1746 (2015).
17. G. Marrone, V. H. Shah, J. Gracia-Sancho, Sinusoidal communication in liver fibrosis and regeneration. *J. Hepatol.* **65**, 608–617 (2016).
18. R. S. McCuskey, Sinusoidal endothelial cells as an early target for hepatic toxicants. *Clin. Hemorheol. Microcirc.* **34**, 5–10 (2006).
19. R. S. McCuskey, The hepatic microvascular system in health and its response to toxicants. *Anat. Rec. (Hoboken)* **291**, 661–671 (2008).
20. L. D. DeLeve, H. M. Shulman, G. B. McDonald, Toxic injury to hepatic sinusoids: Sinusoidal obstruction syndrome (veno-occlusive disease). *Seminars Liver Dis.* **22**, 27–42 (2002).
21. X. Wang, G. C. Kanel, L. D. DeLeve, Support of sinusoidal endothelial cell glutathione prevents hepatic veno-occlusive disease in the rat. *Hepatology* **31**, 428–434 (2000).
22. L. D. DeLeve, R. S. McCuskey, X. Wang, L. Hu, M. K. McCuskey, R. B. Epstein, G. C. Kanel, Characterization of a reproducible rat model of hepatic veno-occlusive disease. *Hepatology* **29**, 1779–1791 (1999).
23. Y. Ito, N. W. Bethea, E. R. Abril, R. S. McCuskey, Early hepatic microvascular injury in response to acetaminophen toxicity. *Microcirculation* **10**, 391–400 (2003).
24. R. S. McCuskey, N. W. Bethea, W. M. K. McCuskey, E. R. Abril, X. Wang, Y. Ito, L. D. DeLeve, Ethanol binge exacerbates sinusoidal endothelial and parenchymal injury elicited by acetaminophen. *J. Hepatol.* **42**, 371–377 (2005).
25. Y. Ito, E. R. Abril, N. W. Bethea, M. K. McCuskey, C. Cover, H. Jaeschke, R. S. McCuskey, Mechanisms and pathophysiological implications of sinusoidal endothelial cell gap formation following treatment with galactosamine/endotoxin in mice. *Am. J. Physiol. Gastrointest. Liver Physiol.* **291**, G211–G218 (2006).
26. L. D. DeLeve, X. Wang, J. Tsai, G. Kanel, S. Strasberg, Z. A. Tokes, Sinusoidal obstruction syndrome (veno-occlusive disease) in the rat is prevented by matrix metalloproteinase inhibition. *Gastroenterology* **125**, 882–890 (2003).
27. T. Kato, Y. Ito, K. Hosono, T. Suzuki, H. Tamaki, T. Minamoto, S. Kato, H. Sakagami, M. Shibuya, M. Majima, Vascular endothelial growth factor receptor-1 signaling promotes liver repair through restoration of liver microvasculature after acetaminophen hepatotoxicity. *Toxicol. Sci.* **120**, 218–229 (2011).
28. A. Benedicto, I. Romayor, B. Arteta, Role of liver ICAM-1 in metastasis. *Oncol. Lett.* **14**, 3883–3892 (2017).
29. K. Szafranska, L. D. Kruse, C. F. Holte, P. McCourt, B. Zapotoczny, The whole story about fenestrations in LSEC. *Front. Physiol.* **12**, 735573 (2021).
30. Y. Kondo, K. Wada, Intrahepatic metastasis of hepatocellular carcinoma: A histopathologic study. *Human Pathol.* **22**, 125–130 (1991).
31. Y. Chan, J. E. Fish, C. D'Abreo, S. Lin, G. B. Robb, A. M. Teichert, F. Karantzoulis-Fegaras, A. Keightley, B. M. Steer, P. A. Marsden, The cell-specific expression of endothelial nitric-oxide synthase: A role for DNA methylation. *J. Biol. Chem.* **279**, 35087–35100 (2004).
32. H. S. Leong, A. E. Robertson, K. Stoletov, S. J. Leith, C. A. Chin, A. E. Chien, M. N. Hague, A. Ablack, K. Carmine-Simmen, V. A. McPherson, C. O. Postenka, E. A. Turley, S. A. Courtneidge, A. F. Chambers, J. D. Lewis, Invadopodia are required for cancer cell extravasation and are a therapeutic target for metastasis. *Cell Rep.* **8**, 1558–1570 (2014).
33. P. L. Tremblay, J. Huot, F. A. Auger, Mechanisms by which E-selectin regulates diapedesis of colon cancer cells under flow conditions. *Cancer Res.* **68**, 5167–5176 (2008).
34. N. Aceto, A. Bardia, D. T. Miyamoto, M. C. Donaldson, B. S. Wittner, J. A. Spencer, M. Yu, A. Pely, A. Engstrom, H. Zhu, B. W. Brannigan, R. Kapur, S. L. Stott, T. Shioda, S. Ramaswamy, D. T. Ting, C. P. Lin, M. Toner, D. A. Haber, S. Maheswaran, Circulating tumor cell clusters are oligoclonal precursors of breast cancer metastasis. *Cell* **158**, 1110–1122 (2014).
35. M. Cristofanilli, G. T. Budd, M. J. Ellis, A. Stopeck, J. Matera, M. C. Miller, J. M. Reuben, G. V. Doyle, W. J. Allard, L. W. M. M. Terstappen, D. F. Hayes, Circulating tumor cells, disease progression, and survival in metastatic breast cancer. *N. Engl. J. Med.* **351**, 781–791 (2004).
36. L. D. DeLeve, Dacarbazine toxicity in murine liver cells: A model of hepatic endothelial injury and glutathione defense. *J. Pharmacol. Exp. Ther.* **268**, 1261–1270 (1994).
37. L. D. DeLeve, Cellular target of cyclophosphamide toxicity in the murine liver: Role of glutathione and site of metabolic activation. *Hepatology* **24**, 830–837 (1996).
38. L. D. DeLeve, X. Wang, J. F. Kuhlenskamp, N. Kaplowitz, Toxicity of azathioprine and monocrotaline in murine sinusoidal endothelial cells and hepatocytes: the role of glutathione and relevance to hepatic venoocclusive disease. *Hepatology* **23**, 589–599 (1996).
39. B. Joseph, V. Kumaran, E. Berishvili, K. K. Bhargava, C. J. Palestro, S. Gupta, Monocrotaline promotes transplanted cell engraftment and advances liver repopulation in rats via liver conditioning. *Hepatology* **44**, 1411–1420 (2006).
40. R. Fraser, B. R. Dobbs, G. W. Rogers, Lipoproteins and the liver sieve: The role of the fenestrated sinusoidal endothelium in lipoprotein metabolism, atherosclerosis, and cirrhosis. *Hepatology* **21**, 863–874 (1995).
41. H. Nagase, R. Visse, G. Murphy, Structure and function of matrix metalloproteinases and TIMPs. *Cardiovasc. Res.* **69**, 562–573 (2006).
42. G. Bergers, R. Brekken, G. McMahon, T. H. Vu, T. Itoh, K. Tamaki, K. Tanzawa, P. Thorpe, S. Itohara, Z. Werb, D. Hanahan, Matrix metalloproteinase-9 triggers the angiogenic switch during carcinogenesis. *Nature Cell Biol.* **2**, 737–744 (2000).
43. S. Arai, M. Mise, T. Harada, M. Furutani, S. Ishigami, M. Niwano, M. Mizumoto, M. Fukumoto, M. Imamura, Overexpression of matrix metalloproteinase 9 gene in hepatocellular carcinoma with invasive potential. *Hepatology* **24**, 316–322 (1996).
44. A. Hayasaka, N. Suzuki, N. Fujimoto, S. Iwama, E. Fukuyama, Y. Kanda, H. Saisho, Elevated plasma levels of matrix metalloproteinase-9 (92-kd type IV collagenase/gelatinase B) in hepatocellular carcinoma. *Hepatology* **24**, 1058–1062 (1996).
45. J. Yan, M. J. Smyth, M. W. L. Teng, Interleukin (IL)-12 and IL-23 and their conflicting roles in cancer. *Cold Spring Harb. Perspect. Biol.* **10**, a028530 (2018).
46. M. Introna, A. Mantovani, Early activation signals in endothelial cells. Stimulation by cytokines. *Arterioscler. Thromb. Vasc. Biol.* **17**, 423–428 (1997).
47. J. A. Lawson, A. Farhood, R. D. Hopper, M. L. Bajt, H. Jaeschke, The hepatic inflammatory response after acetaminophen overdose: Role of neutrophils. *Toxicol. Sci.* **54**, 509–516 (2000).
48. F. Otaka, Y. Ito, S. Nakamoto, N. Nishizawa, T. Hyodo, K. Hosono, M. Majima, W. Koizumi, H. Amano, Macrophages contribute to liver repair after monocrotaline-induced liver injury via SDF-1/CXCR4. *Exp. Ther. Med.* **22**, 668 (2021).
49. S. E. Goldblum, X. Ding, J. Campbell-Washington, TNF-alpha induces endothelial cell F-actin depolymerization, new actin synthesis, and barrier dysfunction. *Am. J. Physiol.* **264**, C894–C905 (1993).
50. A. K. Hubbard, R. Rothlein, Intercellular adhesion molecule-1 (ICAM-1) expression and cell signaling cascades. *Free Radic. Biol. Med.* **28**, 1379–1386 (2000).
51. S. Sakurada, T. Kato, T. Okamoto, Induction of cytokines and ICAM-1 by proinflammatory cytokines in primary rheumatoid synovial fibroblasts and inhibition by N-acetyl-L-cysteine and aspirin. *Int. Immunol.* **8**, 1483–1493 (1996).
52. Y. C. Lin, C. T. Shun, M. S. Wu, C. C. Chen, A novel anticancer effect of thalidomide: Inhibition of intercellular adhesion molecule-1-mediated cell invasion and metastasis through suppression of nuclear factor-kappaB. *Clin. Cancer Res.* **12**, 7165–7173 (2006).
53. A. A. Tempia-Caliera, L. Z. Horvath, A. Zimmermann, T. T. Tihanyi, M. Korc, H. Friess, M. W. Büchler, Adhesion molecules in human pancreatic cancer. *J. Surg. Oncol.* **79**, 93–100 (2002).
54. H. Shinkawa, S. Tanaka, D. Kabata, S. Takemura, R. Amano, K. Kimura, M. Kinoshita, S. Kubo, The prognostic impact of tumor differentiation on recurrence and survival after resection of hepatocellular carcinoma is dependent on tumor size. *Liver Cancer* **10**, 461–472 (2021).
55. M. Sato, T. Matsubara, J. Adachi, Y. Hashimoto, K. Fukamizu, M. Kishida, Y. A. Yang, L. A. Wakefield, T. Tomonaga, Differential proteome analysis identifies TGF-β-related pro-metastatic proteins in a 4T1 murine breast cancer model. *PLOS ONE* **10**, e0126483 (2015).
56. T. Ogawa, M. Enomoto, H. Fujii, Y. Sekiya, K. Yoshizato, K. Ikeda, N. Kawada, MicroRNA-221/222 upregulation indicates the activation of stellate cells and the progression of liver fibrosis. *Gut* **61**, 1600–1609 (2012).
57. E. Wisse, F. Braet, H. Duimel, C. Vreuls, G. Koek, S. W. Olde Damink, M. van den Broek, B. de Geest, C. H. Dejong, C. Tateno, P. Frederix, Fixation methods for electron microscopy of human and other liver. *World J. Gastroenterol.* **16**, 2851–2866 (2010).
58. F. Cabral, C. M. Miller, K. M. Kudrma, B. E. Hass, J. G. Daubendiek, B. M. Kellar, E. N. Harris, Purification of hepatocytes and sinusoidal endothelial cells from mouse liver perfusion. *J. Vis. Exp.* 56993 (2018).
59. M. Toth, A. Sohail, R. Fridman, Assessment of gelatinases (MMP-2 and MMP-9) by gelatin zymography. *Methods Mol. Biol.* **878**, 121–125 (2012).
60. P. J. Johnson, S. Berhane, C. Kagebayashi, S. Satomura, M. Teng, H. L. Reeves, J. O'Beirne, R. Fox, A. Skowronska, D. Palmer, W. Yeo, F. Mo, P. Lai, M. Iñárraiaegui, S. L. Chan, B. Sangro, R. Miksad, T. Tada, T. Kumada, H. Toyoda, Assessment of liver function in patients with hepatocellular carcinoma: A new evidence-based approach-the ALBI grade. *J. Clin. Oncol.* **33**, 550–558 (2015).

Acknowledgments: We would like to express our deepest appreciation to L. M. Wakefield (NCI, NIH) who provided the 4T1 cells, to the research support platform of Osaka Metropolitan University Graduate School of Medicine for technical assistance, and to Nishimura International Scholarship Foundation. We would also like to thank Bioscience writers (www.biosciencewriters.com/) for English editing. This work was supported by Innovative Areas-Resource and technical support platforms for promoting research “Advanced Bioimaging Support” (JP16H06280), and we would like to thank K. Ota for assistance with EM image acquisitions for 3D-TR and helpful discussion. **Funding:** This work was supported by a JSPS KAKENHI Grant-in-Aid for Scientific Research (C) JP21K07968 for M.S.-M. and T.M.; a Grant-in-Aid for Scientific Research from JSPS (JP19H03641 for M.S.-M., L.T.T.T., H.H., and N.K.; JP20H04110 for N.K.; a Grant for Research Program on Hepatitis from the Japan Agency for Medical

Research and Development (AMED) JP22fk0210107 for M.S.-M., L.T.T.T., H.H., and N.K.; and AMED-CREST JP21gm1010009 for M.S.-M., R.Y., N.O., and N.K. **Author contributions:** T.H.H., M.S.-M., T.M., J.G.-S., and N.K. designed the experiments and interpreted the results. H.Y., A.D., H.U., D.M.P., N.V.H., V.N.H., D.V.H., R.Y., Y.O., and N.Q.D. conducted the experiments. H.S., S.K., M.E., and A.T. were involved in patient recruitment and provided samples from study and diagnostic repositories. T.H.H., M.S.-M., and H.I. analyzed the data. T.H.H., M.S.-M., L.T.T.T., H.H., Y.Y., N.O., K.I., M.E., A.T., K.Y., J.G.-S., and N.K. wrote and revised the manuscript. **Competing interests:** The authors declare that they have no competing interests. **Data and materials**

availability: All data needed to evaluate the conclusions in the paper are present in the paper and/or the Supplementary Materials. All the sequencing data are deposited into the GEO (GSE202457).

Submitted 12 February 2022

Accepted 4 August 2022

Published 28 September 2022

10.1126/sciadv.abo5525

Cancer cells produce liver metastasis via gap formation in sinusoidal endothelial cells through proinflammatory paracrine mechanisms

Truong Huu Hoang, Misako Sato-Matsubara, Hideto Yuasa, Tsutomu Matsubara, Le Thi Thanh Thuy, Hiroko Ikenaga, Dong Minh Phuong, Ngo Vinh Hanh, Vu Ngoc Hieu, Dinh Viet Hoang, Hoang Hai, Yoshinori Okina, Masaru Enomoto, Akihiro Tamori, Atsuko Daikoku, Hayato Urushima, Kazuo Ikeda, Ninh Quoc Dat, Yutaka Yasui, Hiroji Shinkawa, Shoji Kubo, Ryota Yamagishi, Naoko Ohtani, Katsutoshi Yoshizato, Jordi Gracia-Sancho, and Norifumi Kawada

Sci. Adv., **8** (39), eabo5525.
DOI: 10.1126/sciadv.abo5525

View the article online

<https://www.science.org/doi/10.1126/sciadv.abo5525>

Permissions

<https://www.science.org/help/reprints-and-permissions>

Use of this article is subject to the [Terms of service](#)

Science Advances (ISSN) is published by the American Association for the Advancement of Science. 1200 New York Avenue NW, Washington, DC 20005. The title *Science Advances* is a registered trademark of AAAS.
Copyright © 2022 The Authors, some rights reserved; exclusive licensee American Association for the Advancement of Science. No claim to original U.S. Government Works. Distributed under a Creative Commons Attribution NonCommercial License 4.0 (CC BY-NC).